



HAL
open science

Study of Hyper-Saline Deposits and Analysis of their Signature in Airborne and Spaceborne SAR Data: Example of Death Valley, California

Y. Lasne, Philippe Paillou, Anthony Freeman, Tom Farr, Mcdonald Kyle,
Gilles Ruffié, Jean-Marie Malézieux, Bruce Chapman

► **To cite this version:**

Y. Lasne, Philippe Paillou, Anthony Freeman, Tom Farr, Mcdonald Kyle, et al.. Study of Hyper-Saline Deposits and Analysis of their Signature in Airborne and Spaceborne SAR Data: Example of Death Valley, California. IEEE Transactions on Geoscience and Remote Sensing, 2009, 47 (8), pp.2581-2598. hal-00405373

HAL Id: hal-00405373

<https://hal.science/hal-00405373>

Submitted on 12 May 2010

HAL is a multi-disciplinary open access archive for the deposit and dissemination of scientific research documents, whether they are published or not. The documents may come from teaching and research institutions in France or abroad, or from public or private research centers.

L'archive ouverte pluridisciplinaire **HAL**, est destinée au dépôt et à la diffusion de documents scientifiques de niveau recherche, publiés ou non, émanant des établissements d'enseignement et de recherche français ou étrangers, des laboratoires publics ou privés.

Study of Hyper-Saline Deposits and Analysis of their Signatures on Airborne and Spaceborne SAR Data: Example of Death Valley, California

Yannick Lasne, Philippe Paillou, Anthony Freeman, *Fellow, IEEE*, Tom Farr, Kyle McDonald, *Senior Member, IEEE*, Gilles Ruffié, Jean-Marie Malézieux, and Bruce Chapman

Abstract— Field measurements of dielectric properties of hyper-saline deposits were realized over an arid test site located in Death Valley (CA). The dielectric constant of salt and water mixtures is usually high, but can show large variations depending on the salt considered. We confirmed values observed on the field with laboratory measurements, and we used these results in order to model both the amplitude and phase behaviors of the SAR signal, at C-, and L-bands. These analytical simulations allow to reproduce specific copolar signatures observed on both AIRSAR and SIR-C/X-SAR data corresponding to the saltpan of Cottonball Basin. More precisely, the main objective of the present study is to understand the influence of soil salinity as a function of soil moisture on the dielectric behavior of soils and then on the backscattering coefficients recorded in airborne and spaceborne SAR images. We also aimed at proposing the copolarized backscattering ratios and phase differences as indicators of moistened and salt-affected soils. More precisely, we will show that such copolar indicators should allow to follow the seasonal variations of the dielectric properties of saline deposits at both L- and C-band frequencies. Because of the frequency dependence of the ionic conductivity, we also demonstrate that L-band SAR systems should be efficient tools for detecting both soil moisture and salinity while C-band SAR are shown to be more suitable for monitoring of soil moisture only. Our results can be of interest not only to help detecting and monitoring soil moisture in arid environments using orbital SAR, but also to define the future SAR systems dedicated to planetary missions such as the Martian exploration.

Manuscript received XX XX, 2008; revised XX XX, 2008. This work was carried out at the Astronomical Observatory of Bordeaux (OASU) and at the Ecole Nationale Supérieure de Chimie Physique de Bordeaux (ENSCPB), Bordeaux, France. Portions of this work were also carried out at the Jet Propulsion Laboratory, California Institute of Technology, under contract to the National Aeronautics and Space Administration (JPL/CALTECH/NASA).

Y. Lasne, and Ph. Paillou are with the Observatoire Aquitain des Sciences de l'Univers, L3AB-UMR 5804, 33270 Floirac, France (e-mail: lasne@enscpb.fr; paillou@obs.u-bordeaux1.fr).

A. Freeman, T. Farr, K. McDonald, and B. Chapman are with the Jet Propulsion Laboratory, California Institute of Technology, Pasadena, CA 91109-8001, USA (e-mail: tony.freeman@jpl.nasa.gov; tom.farr@jpl.nasa.gov; kyle.mcdonald@jpl.nasa.gov; bruce.chapman@jpl.nasa.gov).

G. Ruffié is with the Ecole Nationale Supérieure de Chimie Physique de Bordeaux, IMS-UMR5218, 33607 Pessac, France (e-mail: g.ruffie@enscpb.fr).

J.-M. Malézieux is with the EGIG – Bordeaux 3 Institute, 33607 Pessac, France (e-mail: jmmalez@egid.u-bordeaux.fr).

Index Terms—AIRSAR, evaporites, copolarized phase difference, IEM, polarimetry, radar backscattering ratio, salinity, SAR, soil moisture, SIR-C/X-SAR.

I. INTRODUCTION

SALINIZATION concerns today an ever-growing part not only for economical issues but also for ecological matters such as: 1) desertification; 2) biomass reduction; 3) degradation of arable lands preventing the development of sustainable agriculture, particularly in arid and semi-arid regions.

Although numerous papers dealt with the relationship between the dielectric properties and moisture content of soils at microwave frequency [1]-[8], few attempts have been made on the salinity effects on the soil complex permittivity.

Nevertheless some studies focusing on the establishment of dielectric mixing models from laboratory measurements taken into account the salinity effect can be found in the literature [9]-[20]. Based on measurements performed at millimeters and centimeters wavelengths on sodium chloride (NaCl) solutions, Lane and Saxton [9] discussed the necessity to take into account the ionic conductivity [21]-[23] produced by an electrolyte in the estimation of the complex permittivity of moist salinized soils derived from the Debye's theory. Assuming the formulation of the relaxation time and ionic conductivity of aqueous NaCl solutions as described by Weil [10] and Cox [11], Stogryn [12] proposed a dielectric mixing model for saline water represented by an equation of the Debye form in which the dielectric parameters are given as functions of water temperature and salinity. Based on the Stogryn's model, Carver [13] investigated the effect of salinity on the complex permittivity. According to him, the microwave response to soil salinity depends upon the density of free ions in the soil. He also stated that such a response is significant for frequencies approximately below 5GHz. Describing the soil as a multiphase mixture of solid particles, water, air voids and salts, Wang [1] introduced the formalism of the transition moisture separating to states of water referred as bound and free water. These states allow to take

into account the density of free ions (due to the occurrence of saline minerals) in solution. Below the transition moisture, the water is assumed to be bound to the soil particles and has shown to have the same dielectric properties of ice ones. On the contrary, exceeding the transition moisture leads to free water component allowing the occurrence of free ions in solution. As a result, the dielectric properties of free water are salinity-dependent because of ionic conductivity corresponding to the mobility of ions in solution [20], [23]. Moreover, in presence of free water, the dielectric properties have shown to be frequency dependent [17], [19], [20] because of the dependence of the ionic conductivity on the frequency [21], [22]. Sreenivas [14] has also conducted an extensive study at L-band over three soils of different textures in order to investigate the influence of salinity and sodicity on the complex dielectric behavior of soils as a function of volumetric soil moisture.

All these different models led to the same conclusion, which is the real part of the dielectric constant decreases whereas the imaginary part increases with increment in salinity. The real part appears to be more dependent on soil moisture while the imaginary part is sensitive to soil salinity.

Because of the differential behavior of the real and imaginary parts of the complex permittivity, microwaves appear to be efficient in detecting soil salinity. While the real part is independent of soil salinity, the imaginary part is highly sensitive to variations in ionic conductivity [12]-[14], [17]-[20]. This allows thus to separate saline soils from others [14].

In microwave remote sensing, it is now well known that the radar backscattering coefficient of a target is highly sensitive to the electrical properties of the target through the permittivity and the conductivity, that is the complex dielectric constant of the material [2], [24]-[25]. If the influence of moisture on backscattering coefficient has been extensively investigated over the last two decades [26]-[34], few theoretical attempts have been performed in order to describe the effect of salinity on the radar backscattering [14], [18], [20], [35]-[36]. Moreover, very little verification has been performed on the large amount of available SAR data (ERS, JERS, RADARSAT, SIR-C/X-SAR, AIRSAR, and ALOS/PALSAR) [35]-[38]. Based on laboratory measurements, Shao [37] confirmed that the frequency and the salinity of soils have little influence on the real part of the dielectric constant while the imaginary part is strongly affected by both salinity and moisture of soil samples, especially in the [1-6GHz] frequency range. Assuming RADARSAT-1 images, these authors also highlighted a strong correlation between the backscattering coefficients extracted from SAR data and the imaginary part of the complex permittivity simultaneously measured on the soil samples of the illuminated scene. More recently, assuming RADARSAT-1 images acquired over the Wadi El-Natron test site (Egypt), Aly [35] proposed a parametric formulation in

order to evaluate the ability of RADARSAT-1 SAR system to monitor the salt content of soils by means of the combination of three SAR modes (S1, S3, and S5) without any use of backscattering models.

According to that, the main objective of the present study is to understand the influence of soil salinity as a function of soil moisture on the dielectric behavior of soils and then on the backscattering coefficients recorded in airborne and spaceborne SAR images. Based on SIR-C/X-SAR and AIRSAR data acquired over the suitable saltpan of the Cottonball Basin test site located in Death Valley (CA), we also aimed at proposing radiometric and phasimetric indicators of moistened and salt-affected soils in terms of the copolarized backscattering ratios and phase differences respectively. More precisely, we will show that such copolar indicators should allow to follow the seasonal variations of the dielectric properties of saline deposits at both L- and C-band frequencies.

For that matter, we first provide a complete description of the geological and meteorological context corresponding to the Cottonball Basin test site located in Death Valley (Section II). Such a description is helpful to provide a better understanding of the salt deposits formation as well as a more precise knowledge of the salt mineral species encountered over the saltpan. Since the amount of saline ions in solution depends upon the moisture content, it also appears essential to understand the climate and hydrological cycles occurring over the test site since the rainfall and evaporation phenomenon govern the variations in the moisture content of soils and then the variations in the dielectric properties of the saltpan.

In order to assess the influence of different salt species on the dielectric properties of the saltpan, we have also conducted both fieldwork and laboratory measurements of the complex permittivity of soil samples (Section III). For that matter, we described the acquisition procedure as well as the vectorial network analyzers considered. The fieldwork measurements revealed the occurrence of several types of salt among which the main contributor lies in the sodium (NaCl) and potassium (KCl) chlorides. Since the dielectric properties of NaCl has been well investigated [9]-[14], [17], [20]-[21], [37], we focused here on the KCl dielectric properties as function of moisture content and frequency in order to experimentally infer the KCl impact on the complex permittivity as observed during the fieldwork campaign.

Afterwards, we present a SAR data analysis derived from temporal series of airborne and spaceborne SAR systems, AIRSAR and SIR-C/X-SAR sensors respectively (Section IV). We showed that the saline deposits present a specific signature when considering the copolarized backscattering ratio and phase difference. We also discovered a variation of such copolar parameters at a seasonal scale. In order to relate such variations to the variations of the dielectric properties, we then performed analytical simulations of the copolarized

parameters by means of the IEM model [27], [39]-[42] with the experimental complex permittivity as input parameters (Section V). If good agreement were found between the simulated and measured copolarized ratio and phase, their variations were correlated to the strong variations of the imaginary part of the complex permittivity due to the high dependence of the imaginary part to the salinity.

Compared to SAR data analysis, the IEM simulations confirm the salinity as the main contributor in the variations of the copolarized ratio and phase difference because of the strong impact of the ionic conductivity on the imaginary part of the complex permittivity. These results are also of great interest not only for the detection and mapping of saline deposits, but also in the monitoring of soils moisture since the salinity effect is closely related to the moisture content. Actually, an important issue of this paper lies in the close relation existing between the copolar parameters and the salinity through the moisture content. We showed that the higher is the soil moisture content of saline deposits, and the higher is the free water component leading to the occurrence of high amounts of mobile ions in solution. It then results in a high ionic conductivity leading to high values of the imaginary part of the complex permittivity. Because of the frequency dependence of the ionic conductivity, we also demonstrate that L-band SAR systems should be efficient tools for detecting both soil moisture and salinity while C-band SAR are shown to be more suitable for monitoring of soil moisture only. It should be pointed out that the guideline of the present work is to help to a better interpretation of spaceborne and airborne SAR data in relation with evaporitic environments which could be of great interest for defining future planetary missions, especially when dealing with the exploration of Mars [43]-[46].

II. THE HYDROLOGIC BASIN OF DEATH VALLEY

A. General Geology

The Death Valley is a hydrologic basin located at the south edge of the Great Basin in the south-eastern California (close to the Nevada/California State boundary). The bordering consolidated rocks mostly result in Precambrian schist and gneiss (consisting of quartz, plagioclase and potassium feldspar), and Paleozoic sedimentary rocks (consisting mostly in carbonate rocks) which compose (1) the Grapevine and Funeral Mountains (Paleozoic and late Proterozoic sedimentary rocks consisting in dolomite, limestone and quartzite) at the north and north-eastern margin of the basin, (2) portions of the Panamint Range (late Precambrian and Paleozoic) along the western valley margin, as well as (3) much of the Black Mountains Range (Late Proterozoic metamorphic rocks consisting in metadiorite) along the south-eastern margin (**Fig. 1**) [47]-[50].

The overlying valley fills are mostly Tertiary (volcanic and sedimentary rocks) and Quaternary (gravels, fine-grained alluvial, and playa deposits) formations. The Quaternary deposits are the most significant to the hydrology of the bottom of the basin, namely the saltpan of the Death Valley which is one of the greatest world's salt pans. In the central part of Death Valley, the saltpan lies at 282 feet (85.5m) below the sea level while salt deposits (evaporitic minerals) form a crust covering more than 200 square miles (more than 320 square kilometers). The thickness of the salt crust ranges from several millimeters to more than one meter. Under the crust are clastic sediments such as silt and clay [47], [51]-[52].

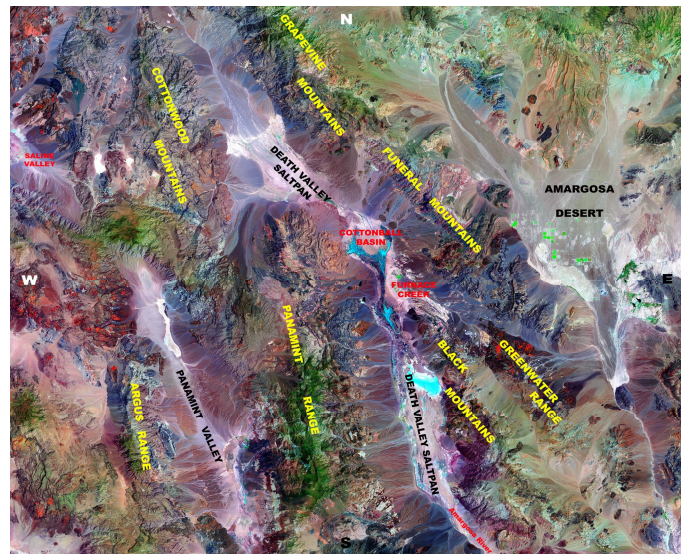


Fig. 1: Map of the Death Valley indicating the most important geological formations under consideration. This map is superimposed to acquisitions performed with the Enhanced Thematic Mapper Plus (ETM+) sensor onboard the Landsat 7 satellite.

B. Climatic and Weather Conditions in Death Valley

The extreme climatic conditions of Death Valley derives from high temperatures (commonly exceeding 120°F - 48.9°C- during the summer months) which, combined with high wind movement (especially during spring months), lead to high evaporation rates, the highest in the United States as recorded by official weather stations [52]-[54].

Coupled to low rainfall and humidity, such extreme conditions make the hydrologic basin of Death Valley as one of the hottest and driest places in the world.

Table I displays the weather and climatic information of the Death Valley in terms of temperature, rainfall, wind movement, humidity and evaporation rate, which all are derived from data recorded by official weather stations from the U.S. Weather Bureau [52]-[54].

As reported in Table I, temperatures in Death Valley display monthly average values of about 65-70°F (18-21°C)

TABLE I

MONTHLY AVERAGE PRECIPITATION (P), EVAPORATION RATE (EvR), MAXIMUM TEMPERATURE (T°), HUMIDITY (H), AND WIND MOVEMENTS (W) RECORDED OVER THE SALTPAN OF THE COTTONBALL BASIN LOCATED IN DEATH VALLEY, CA. DATA FROM PUBLICATIONS OF U.S. WEATHER BUREAU ACCORDING TO THE FURNACE CREEK AND COW CREEK STATIONS. VALUES ARE EXPRESSED IN ENGLISH UNITS (INCHEES, DEGRESS °F, AND MILES).

Month	P	P	P	EvR	T°	T°	H (in %)	W (in miles)
	Furnace Creek (1912-1959)	Furnace Creek (1961-2005)	Cow Creek (1912-1959)	of saltpan (1958-1961)	Furnace Creek (1911-1952)	Furnace Creek (1961-2005)	Cow Creek (1958-1961)	Saltpan (1958-1961)
January	0.23	0.28	0.19	3.21	64.9	66.2	27.2	446
February	0.29	0.43	0.38	5.62	72.3	73.4	25.9	1269
March	0.17	0.28	0.19	10.25	80.4	81.1	14.0	1375
April	0.11	0.13	0.20	14.08	89.6	89.7	12.5	1725
May	0.07	0.06	0.10	17.25	99.1	99.5	14.5	1661
June	0.02	0.06	0.02	21.37	110.4	108.7	11.4	1640
July	0.08	0.13	0.12	22.14	116.4	115.6	11.3	1369
August	0.12	0.15	0.15	20.17	113.7	113.8	16.0	1485
September	0.11	0.21	0.13	15.36	105.5	105.8	15.8	1278
October	0.10	0.11	0.16	10.71	90.3	92.9	15.7	1134
November	0.15	0.19	0.15	5.13	75.6	76.3	20.1	602
December	0.21	0.18	0.38	3.94	65.8	65.2	26.1	1105

in winter and 110-115°F (43-46°C) in summer. Higher temperatures may be expected over the saltpan during summer months from May through September (July being the hottest). As an example, the highest official record in the hydrologic basin was recorded at a blazing 134 °F (57 °C), just after the Libyan record at a 136 °F (58 °C) temperature.

As the rainfall is concerned, the Furnace Creek Ranch (see Fig. 1) displays the lowest annual average rainfall of any recorded places in the United States (1.66 inches -4.2cm- per year) since most rainfall is blocked by the Sierra Nevada Mountains to the west accounting for the extreme aridity of Death Valley [52]-[54]. Table I reports the annual precipitation averaged over 47 and 44 years of the [1912-1959] and [1961-2005] periods respectively. It can be seen that the precipitation is greater during the winter months of December, January, and February, then declines to a low point in summer months (June and July). Since these records are averaged on sufficiently long periods, they provide a highly confident indicator of the yearly distribution of precipitation over the basin.

Based on official records reported in Table I, it may be seen that the humidity of the hydrologic basin is higher during the winter months from November to February (with an annual average humidity about 25%), whereas the spring and summer months (April to July) record the lowest values of about 12%. In parallel, it may also be seen that the months of April, May, and June are the windiest of the year while November, December, and January are the calmest.

Dealing with the evaporation, Kohler [53] reported evaporation rates of more than 120 inches (3.05m) per year over most of the hydrologic basin. The values recorded by the U.S. Weather Bureau between 1958 and 1961 indicate an average evaporation rate of 149 inches (3.79m) per year as reported in Table I. Nevertheless, according to recent records,

the evaporation rate is assessed at 128 inches (3.25m) annually, which is 58 times the precipitation rate if we assume the recent 44-year average annual rainfall rate of 2.21 inches (5.4cm). According to the averaged values of the evaporation rates recorded over the saltpan, the evaporation appears to be lower in winter (from November to February) and greater during the summer months (from May to August). Such observations highlight a steeply close correlation of evaporation rate with temperature, wind movements and rainfall, as well as humidity. Actually, during the summer months, the high temperatures combined to high wind movements and low rainfalls in the same time, logically lead to high evaporation rates. On the opposite, these rates decrease in winter since the temperatures and the wind movements are lower while the rainfalls increase. Because such climatic and weather conditions prevail most of the time in Death Valley, they account for the recorded high evaporation rates.

C. Hydrology and Drainage Systems

Death Valley is the terminal discharge point for 27 hydrographical areas, with a surface area of about 15,800 square miles (40,922 km²). Recharge to the basin mainly derives from the percolation of streams or storm runoff from the bordering mountains reaching the saltpan by crossing the gravel fans, and then reaching the saltpan as ground water. Among the hydrographical areas, five main drainage systems can be distinguished [47], [52].

Subsurface inflows, originating from the Amargosa River drainage system, discharges into the south end of the Death Valley saltpan. Although the main stems of the Amargosa River lies in the lake beds at Tecopa, this drainage system

may also receive some ground water inflows from the Mojave River drainage system on the south. Except during wet periods, only short stretches of the Amargosa River are perennial and surface water flows rarely occur. The total drainage area is about 6000 square miles (15540 km²).

Draining the northwest arm of the Death Valley, the Salt Creek drainage basin originates in the Furnace Creek Formation over an area of about 1600 square miles (4144 km²), which is mostly mountainous. Since the mountains are composed largely of Paleozoic carbonate rocks and are without perennial streams, the water collected result from storm runoff in the bordering mountains.

Water discharging from the east slope of the Panamint Range drains to the saltpan in a series of mountain valleys leading to a 450 square miles (1165 km²) drainage area. The water collected issued from hard rains, drains to the saltpan through fractures and channels from the bedrock formations in the mountains allowing movement of ground water. There is no perennial stream and the surface water discharging from the mountains onto the gravel fans seeps into the gravels, even floods resulting from torrential events.

With a total drainage area of about 200 square miles (518 km²), the Black Mountains drains to the Death Valley saltpan through a series of cascading gorges. There are no perennial streams. Although the Black Mountains are mainly composed of Precambrian crystalline rocks (south half), the north half consist of Tertiary volcanic rocks and sediments. As a result, each gorge discharges at the foot of the mountains onto steep alluvial fans, and much of the discharged runoff continues to the saltpan.

The west slope of the Funeral Mountains drains directly to the Death Valley saltpan while the east slope drains in the Amargosa Desert. The draining area covers about 200 square miles with water discharging onto alluvial gravels sloping to Cottonball Basin.

Finally, ground water also probably enters the basin from three neighboring drainage basins: The Pahrump Valley on the southeast, the Sarcobatus Flat on the north, and the Amargosa Desert on the east contribute additional recharges.

Surface and ground water drainages move towards the Death Valley saltpan where discharge occurs through evaporation.

D. Geochemistry of the Saltpan

As mentioned above, the Quaternary deposits that are significant in the hydrology of the saltpan include salt deposits and saliferous playas sediments that cover more than 200 square miles (518 km²) in the central part of Death Valley [51]-[52].

As the chemical composition of the saltpan is concerned, it is closely related to the water inflows because of the leaching from the bordering mountains. Since the largest springs result

from the Black Mountains and the Funeral Mountains (because discharging along high-angle faults) with flows more than 2550 gpm –gallons per minute i.e. 11600 liters per minute- (according to the sum of Travertine, Nevares, and Texas Springs), such water discharges strongly influence the geochemistry of the saltpan. Moreover, since these leaching waters usually discharge onto the alluvial gravels at the foot of the mountains, most of this water is saline. According to several analysis of the geochemical composition of water inflows performed on the bordering mountains (PR, FM, BM) and Amargosa River, they highlight high chloride salts concentrations (NaCl, KCl and MgCl) [51]-[52]. As an example, even if it has been shown that the spring waters from the Panamint Range are high in sulfates and comparatively low in chlorides and carbonates, the analysis of numerous springs of the Amargosa River show high bicarbonate concentrations. All of the latest are also high in sodium and sulfates, and they present significant proportions of calcium, chlorides, potassium and magnesium [52].

Finally, leading to the largest spring waters, the Black Mountains and the Funeral Mountains predominantly contribute to the geochemistry of the saltpan. Chemical analysis of the spring waters underlined very high concentrations in chlorides and sodium as well as high proportions of sulfate, bicarbonates, potassium, magnesium and calcium [52].



Fig. 2: Moistened saline deposits of sodium chloride observed over the Cottonball Basin in Death Valley, CA: N 36°29'35", W 116°54'47".

It is obvious that surface water and shallow ground water may vary in composition from one part to another part of the saltpan and from time to time because of sources, seasonal temperature changes, water balance (ratio between inflows and outflows) and position in the pan. Nevertheless, the chemical compositions of the Black Mountains and the Funeral Mountains can account for the salt crust in the center of the Death Valley which derives from the precipitation of sodium chloride (*cf.* Fig. 2). Then, according to the solubility properties of salts and the chemical abundances previously

TABLE II
FIELDWORK MEASUREMENTS RESULTS OF COMPLEX DIELECTRIC CONSTANTS PERFORMED OVER THE SALTPAN OF THE COTTONBALL BASIN LOCATED IN DEATH VALLEY, CA (N 36°29'35", W 116°54'47"). RESULTS ARE GIVEN IN $\epsilon' - j\epsilon''$ FORMAT.

Open-ended dielectric probe #1						
Frequency (GHz)	NaCl Crystal Crust (dry)	NaCl Crystal Crust (wet)	Clay Layer (wet)	Clay Layer (wet)	KCl+NaCl Water Layer	River Water (NaCl)
1.5	3.44 – j11.47	8.72 – j38.05	10.13 – j66.86	7.09 – j49.65	3.64 – j42.87	72.42 – j45.24
2.0	3.45 – j8.77	8.94 – j28.97	11.55 – j48.73	8.32 – j36.19	4.62 – j33.14	72.87 – j37.04
5.0	3.19 – j3.75	7.81 – j12.23	9.95 – j16.32	7.82 – j12.64	5.05 – j11.53	56.39 – j26.49
5.5	3.20 – j3.55	7.73 – j11.39	9.34 – j13.94	7.54 – j10.95	4.98 – j10.66	53.18 – j26.07
6.0	3.12 – j3.22	7.45 – j9.76	10.73 – j14.01	8.75 – j11.01	6.21 – j9.47	40.82 – j17.57

Open-ended dielectric probe #2						
Frequency (GHz)	NaCl Crystal Crust (wet)	NaCl Crystal Crust (wet)	Clay Layer (wet)	Clay Layer (wet)	KCl+NaCl Water Layer	River Water (NaCl)
1.5	7.79 – j23.52	10.76 – j32.58	10.92 – j60.84	8.46 – j48.69	4.64 – j41.61	-
2.0	7.10 – j18.27	9.92 – j25.35	10.02 – j43.47	7.85 – j34.75	4.76 – j30.24	-
5.0	5.94 – j9.53	8.59 – j13.47	6.38 – j12.38	5.31 – j9.97	4.40 – j9.34	-
5.5	5.85 – j9.01	8.49 – j12.79	6.02 – j10.66	5.14 – j8.63	4.36 – j8.11	-
6.0	5.65 – j7.94	8.26 – j11.23	7.26 – j10.46	6.42 – j8.57	5.62 – j8.06	-

mentioned, the remainder chloride salts that can be found among clay and silt lay in potassium and magnesium chlorides [20], [52], [55].

Moreover, the basin being isolated, the sedimentary deposits present a typical concentric facies pattern (*bull eye's facies*, cf. [20], and [55] for more details on sedimentary basins) as discussed by [52]: at the center of the pan, the salts in the crust and the brines are mostly chlorides (halite, potassium and magnesium chlorides) which represent the most extensive of the salt zones and covers about half the pan. The chloride zone is surrounded by sulfates, gypsum, and anhydrite which, in turn, are surrounded by slightly soluble salts such as carbonates precipitating at the edge of the pan. Such a zonal arrangement reflects the differences in the solubility of the salts, with the slightly soluble salts precipitating on the edge of the basin, whereas highly soluble salts precipitate in the center of the pan.

As a result of the previous geological, hydrological and chemical observations, during the summer the high temperature and evaporation lead to the vanishing of water inflows as rapidly as it is discharged. Then, the salt crust can be formed resulting from the surface precipitation of sodium chloride and only magnesium and potassium chlorides remain dissolved because of their solubilities. On the contrary, in winter the water balance being positive (inflows exceeds water evaporation), the water spreads over the surface as a thin sheet and collects in shallow pools. In this case, the sodium chloride crust is dissolved by fresh increments of ground water and surface water floods, and mixed with higher soluble salts (potassium and magnesium chlorides) in solution. This surface water usually starts to form in November or December, reaching a maximum in January or

February, and decreases until the end of April or the beginning of May when most of the surface water have entirely disappeared (some moisture content still remain mixed with the underlying clastic sediments: clays and silts).

Then, depending on the dissolved salt occurrences, the complex permittivity of such a media should present strong seasonal variations which may have significant impacts on the backscattering coefficients recorded in temporal series of SAR images, in terms of amplitude as well as copolarized phase difference [20], [39].

III. FIELD AND LABORATORY MEASUREMENTS OF THE COMPLEX PERMITTIVITY

Even if it is well known that roughness impacts the radar backscattering coefficients, we only focused in the following on the dielectric properties of the saline deposits since they are usually smooth especially at the wavelengths under consideration (C-, L-, and P-bands). Nevertheless, it should be noticed that such a hypothesis on the roughness parameters is based on measurements and observations we recently performed on the saltpan in Cottonball Basin with a measured rms-height of 0.3cm and a correlation length of 2.7cm [20].

Then, neglecting the roughness parameters, the main contributor in the radar backscattering response lies in the dielectric properties of the saltpan which are closely related to its mineralogical composition. For that matter we recently performed *in situ* measurements of the dielectric properties of the saltpan over a test site located in Cottonball Basin (N 36°29'35", W 116°54'47", Death Valley, CA) as shown in **Fig. 2** and corresponding to a specific radar signature we

observed on SIR/X-SAR and AIRSAR images as described in the next section.

More precisely, in order to assess the dielectric properties of the observed saline deposits, we have not only conducted laboratory measurements [20] but also fieldwork experiments.

A. Fieldwork experiments conducted over the Cottonball Basin

In order to extract directly on field the dielectric properties of soils, in terms of real and imaginary parts of the complex permittivity, we worked to the development of a measurement technique based on the measurement of the S11 reflection coefficient in amplitude and phase of an electromagnetic wave on a sample surface [56]-[57]. Measurements were carried out by means of a portable vectorial network analyzer (VNA) coupled to an open-ended dielectric probe.

The VNA used is the *Anritsu 2026A* which has been previously calibrated at Jet Propulsion Laboratory (JPL/Caltech) on standard chemical samples following the same calibration procedure as the one reported in [20] and going through 4 steps: (1) the VNA calibration by means of capacitive cells (open, short and broadband load) in order to define a reference plane allowing to prevent measurements errors due to blemishes of both the VNA and the coaxial cable connectors, (2) a reference measurement typically on air that allows to remove the probe effects from the sample measurements, (3) the standardization of the probe on standard chemical samples in order to determine the capacitive parameters of the dielectric probe namely the equivalent capacitance G_0 and the conductance C_0 since the dielectric probe can be represented by a capacitive equivalent circuit [58]-[60], and (4) the sample measurements. All these steps are detailed in [20]. For ease of reference we summarize on the following the main processing steps.

The knowledge of the capacitive parameters of the probe combined with the measurements of the complex reflection coefficients (S11) then makes it possible to invert the dielectric properties of a medium by using a capacitive inversion algorithm. According to [59], it has been shown that the conductance for a SMA-type probe in the [45MHz – 5GHz] frequency range can be expressed as follows:

$$C_0 = C_1 \varepsilon^b \quad (1)$$

while the equivalent capacitance G_0 can be neglected for frequency values such that the coaxial line internal diameter is small compared to the wavelength [56]. In (1), C_1 and b are parameters related to the probe and ε is the complex permittivity of samples. Moreover, since C_0 has been shown to not depend upon frequency for values less than 7GHz [60], the standardization procedure allows assessing the dependency of C_0 on the complex permittivity of the chemical standards for which the variations of the complex dielectric constant with frequency are well known (Smith abacus). As a

result, the C_1 and b parameters can be obtained by means of a linear regression method on the form:

$$\log(C_0) = \log(C_1) + b \log(\varepsilon) \quad (2)$$

Afterwards, the capacitive inversion algorithm consists in defining a relation between the complex permittivity and the reflection coefficients measured on natural samples. Such an algorithm is based on the complex admittance Y of the equivalent capacitive circuit which is inversely proportional to the characteristic capacitor impedance $Z = 1/Y$, where Y can be expressed as function of the probe parameters:

$$Y = j \cdot \omega \cdot C_0 = j \cdot \omega \cdot C_1 \cdot \varepsilon^b \quad (3)$$

ω being the angular frequency. Dealing with the reflection coefficient ρ_{mes} measured on samples, it can be derived from the admittance by:

$$\rho_{mes} = (1 - y)/(1 + y) = |\rho| e^{j\varphi} \quad (4)$$

where y denotes the complex admittance normalized to the characteristic admittance of the coaxial line (Y_0). $|\rho|$ and φ represent respectively the module and the phase of the complex reflection coefficient.

In order to precisely measure the phase associated to the reflection coefficient, ρ_{mes} is normalized to a reference measurement performed on air (ρ_{air}). Finally, the relation between the complex reflection coefficient measured on natural geological samples and their associated complex permittivity can then be expressed as follows:

$$\frac{\rho_{mes}}{\rho_{air}} = \frac{1 - y}{1 + y} \cdot \frac{1 + y_{air}}{1 - y_{air}} = \frac{1 - jC_1 \varepsilon^b \omega Z_0}{1 + jC_1 \omega Z_0} \cdot \frac{1 + jC_1 \omega Z_0}{1 - jC_1 \omega Z_0} \quad (5)$$

From (5), it can be seen that the knowledge of the C_1 and b probe parameters and the characteristic capacitor impedance of the coaxial line (Z_0) makes it possible to invert the complex dielectric properties of natural samples from the measurements of the complex reflection coefficients.

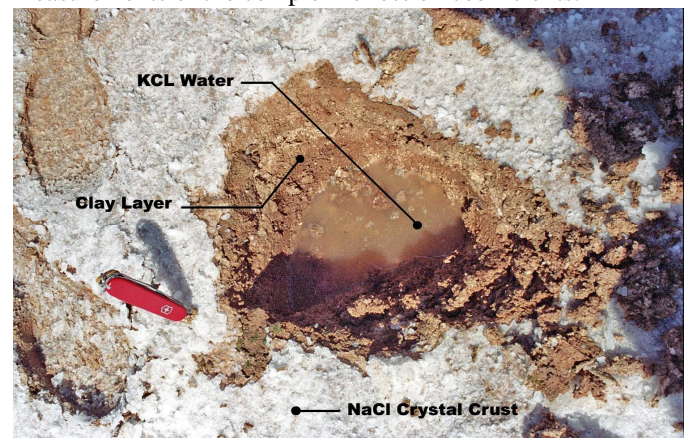


Fig. 3: Hand dug pit performed over the saltpan displaying the main constituents of soil: a NaCl crystal layer (white crust) of few millimeters thick overlies a mixture of clay and loam (brown Clay layer) combined with a KCl saturated aqueous solution.

Following the procedure described above, Table II summarizes the measurements performed over the saltpan in Cottonball Basin. Fig. 3 gives an overview of the main soil

constituents measured on field namely the Sodium Chloride Crystal layer (white crust), the Clay layer which is a mixture of clay and loam (brown layer) and the Water component mainly constituted of dissolved Potassium Chloride salt (sylvite). As the surface NaCl (halite) crust is concerned, its dielectric properties were measured for two different moisture conditions reported in Table II as wet and dry.

The complex permittivity values obtained over the saltpan appear to be coherent with previously published results of the dielectric constant measurements that can be found in the literature [4]-[6] dealing with the salinity effect on the dielectric properties of natural media [13]-[20].

B. Salinity Effect on the Dielectric Constant

The influence of salinity on both the real and the imaginary parts of the dielectric constant can be observed. Actually, as the real part is concerned, the measurements revealed very low values that can be explained by salinity effect since it has been shown that ϵ' decreases with increment of salinity especially for high moisture content [13]-[20]. As an example, the real part for the Sodium Chloride crust displays variations on the order 8-10 at L-band whereas the real part for the KCl/NaCl layer is approximately 3-4 since the higher solubility of the KCl salt compared to NaCl leads to higher salinity values.

On the contrary, the imaginary part ϵ'' is strongly affected by both salinity and mineralogical composition. The high values of ϵ'' recorded during the fieldwork experiment are related to the amount of dissolved salts (concentration of free electrons and ions) controlling the ionic conductivity of soils [20]-[23], [61]: the higher is the amount of mobile ions in solution (usually referred as free water component in the dielectric mixing model [1]), the higher is the ionic conductivity. Since the imaginary part vary linearly with the ionic conductivity, an increase in salinity should then result in an increasing imaginary part, more especially for high water content exceeding the transition moisture value [1], [5], [19]-[20]. Such a behavior can be identified in the measurement results. According to the NaCl salt crust, ϵ'' shows an increase from approximately 10 to the order 25-30 at L-band because of a greater amount of dissolved salts due to the increment in moisture content. Nevertheless, because of the higher solubility of the KCl solution allowing higher amount of dissolved salts compared to NaCl -and then higher ionic conductivity-, ϵ'' displays an increase to about 42 for the KCl/NaCl aqueous solution at the same frequency range. Even higher values of ϵ'' , exceeding 50 at L-band, can be observed for the Clay layer because of the occurrence of highly soluble salts such as potassium and magnesium chlorides as revealed by chemical analysis previously performed over the saltpan and reported in [52].

C. Frequency Effect on the Dielectric Constant

Depending on frequency, the conductivity due to the presence of salts should then introduce a frequency dependence of both the real and imaginary parts of the dielectric constant. According to the real part, it can be observed from the results reported in Table II that the real part slowly decreases in the frequency range under consideration [2GHz-6GHz]. Such a behavior is in good agreement with the ones reported in numerous published papers [1]-[5], [13]-[20], [37], and supports the assumption that the real part of the dielectric constant is mainly affected by the moisture content.

Dealing with the imaginary part, it can be seen that it strongly decreases with increment in frequency because of the dependence of the imaginary part on the ionic conductivity. These measurements results agree well with the ones reported in [2] concerning the sea water by comparison with pure water. According to [18], [20], and [37] the same variations can be observed for ϵ'' derived from experimental measurements performed on NaCl concentrated solutions. Other investigations dealing with kaolinite, montmorillonite, and NaCl led to the same variations of the frequency dependence of the imaginary part [17]. As reported in [20] and [23], these variations can be explained by means of the Debye-Falkenhagen theory [21]-[22] which stipulates that such a variation of ϵ'' with frequency can be attributed to the frequency dependence of the ionic conductivity. Since the ionic conductivity usually describes the mobility of ions in an electrolyte solution, it has been shown that the occurrence of an external electric field (microwave emission) could modify the velocity of the mobile ions through the *electric force of relaxation* [22]. Schematically, the motion of an ion in an electrolyte leads to a dissymmetry of the electronic charge density, resulting in a retarding force (electric force of relaxation) on the mobile ion which decreases its mobility. Typically, assuming a low-frequency oscillating electric field (microwave emission), the mobile ion oscillates. The density of electronic charges is then less asymmetric and the retarding effect is reduced (reduction of electrolyte friction). It results in an increase in the ion mobility and hence an enhancement of the electrolyte conductivity. On the contrary, increasing the frequency will contribute to make the mobile ion oscillating so fast that the net ionic motion is smaller than the one at low frequency. As a result, the electronic force of relaxation vanishes and the electronic density, as well as the mobile ion, can be regarded as motionless. Then, the decrease in the ion mobility leads to the decrease in the conductivity of the electrolyte. Being linearly dependent on the ionic conductivity, the imaginary part of the dielectric constant of such an electrolyte should then decrease with increment in frequency. As an example, the imaginary part of the Clay layer decreases from the range [48.7-66.9] to [8.6-14] when increasing the frequency from 1.5 to 6GHz.

Moreover, such a frequency behavior appears to be moisture dependent. Actually, it can be seen for the NaCl crystal layer that the decrease of ϵ'' in frequency is steeper when considering higher moisture contents. As an example, assuming a dry NaCl crust, ϵ'' decreases from 11.5 to 3.2 in the frequency range [1.5GHz – 6GHz]. Assuming higher water contents (reported as wet crust in Table II), the imaginary part present a steeper decreases from about 23.5-38 to 7.9-11.2. This moisture dependence can be explained by the amount of mobile ions: the higher is the water content, the greater is the amount of mobile ions in the electrolyte, and then the higher is the effect of the ionic conductivity on the imaginary part.

D. Laboratory Measurements performed on KCl

In [20], we presented experimental measurements performed on NaCl solutions mixed with sand corresponding to the Pyla dune test site. Dealing with the Death Valley, we extended the laboratory measurements to the KCl electrolyte since important amounts of potassium chlorides have been observed over the Cottonball Basin.

The dielectric constant measurements on KCl electrolytes were carried out by means of an *Anritsu 37325A* vectorial network analyzer coupled to an open-ended coaxial dielectric probe of SMA type, and connected to an acquisition software. The acquisition procedure is the same than the one used in Death Valley which consists in inverting the complex dielectric properties of natural samples from the measurements of the complex reflection coefficients S11. In order to reduce the measurement errors, the S11 measurements results were averaged on 6 measurements series performed on each sample and for each moisture content value.

Fig. 4 displays measurements results of real and imaginary parts of a 100%-concentrated KCl electrolyte as function of frequency and moisture content in the ranges [500MHz – 7GHz] and [0.05 – 0.6] respectively.

As the real part is concerned, if the measurements results indicate that the real part increases with increment in moisture content, the laboratory results also confirm the frequency dependence of ϵ' observed in measurements performed over the saltpan. Actually, it can be seen that ϵ' slowly decreases with increment in frequency except for high moisture content ($m_v > 0.37$). For instance, assuming a given water content of 30%, ϵ' decreases from 7.7 to 4.6 in the [1.8GHz – 7GHz] frequency range. For very low moisture content ($m_v < 0.15$), ϵ' is not frequency-dependent while for high moisture content values ($m_v > 0.40$), ϵ' shows a stronger decrease from about 23 to about 15 in the [2.2GHz – 7GHz] frequency range. Such results also highlights the occurrence of a transition moisture W_t as suggested by [1] and [6], and measured by [20] for NaCl measurements. Actually, the

transition moisture W_t corresponds to the water content separating two distinct regimes for water referred as bound and free water. In the bound water region, the water being bounded to the soil particles, the dielectric properties of the mixtures have been shown to be close to the ice ones (low loss medium, [1]). On the contrary, exceeding the moisture transition value, the water is referred as free water allowing the occurrence of mobiles ions in the electrolyte and then the influence of salinity through the frequency dependence of the ionic conductivity. Then, according to our laboratory measurements, a transition moisture of $W_t = 0.37$ can be distinguished.

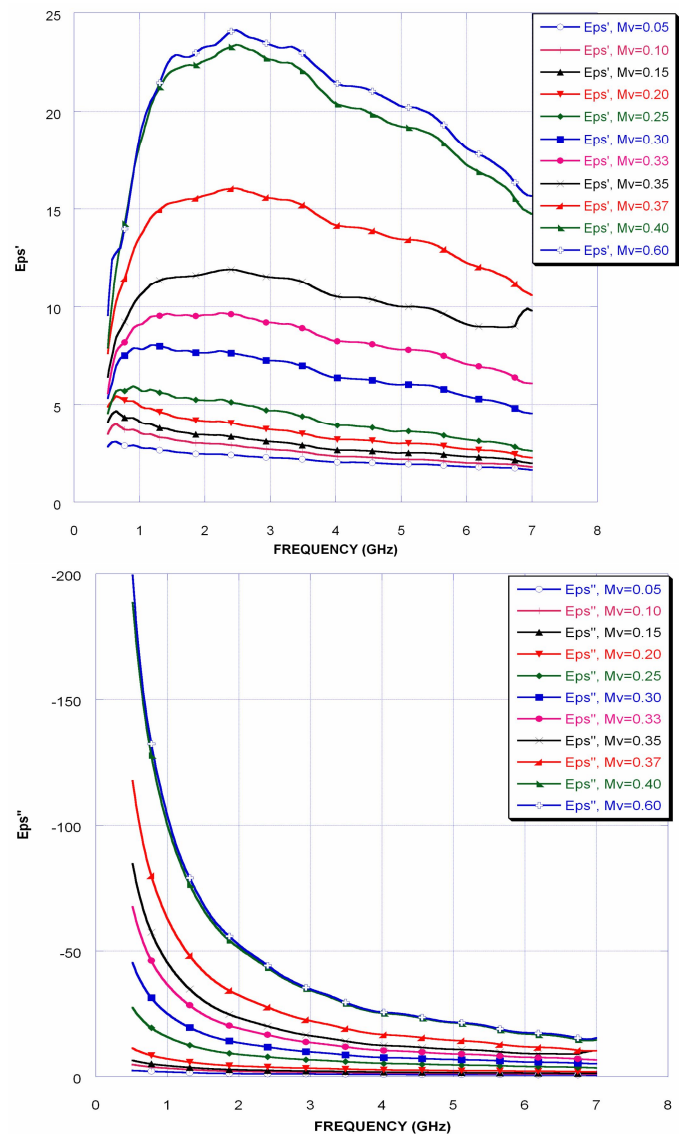


Fig. 4: Frequency dependence of the real (on top) and imaginary (bottom) parts of the complex permittivity of a KCl saline electrolyte for different volumetric water content values ranging from 0.05 to 0.6. The real part is derived from laboratory measurements performed by means of a vectorial network analyzer coupled to an open-ended coaxial dielectric probe for a salinity value of $S = 100\%$. For each water content, the measured complex permittivity is averaged on 6 measurements in order to reduce errors due to vanishes of the instrumentation system.

Moreover our experimental results are also in good agreement with the Debye' theory and support the assumption that the real part of soil permittivity is inversely proportional to the salinity content [4]. Actually, compared to the measurement results reported in [20] and related to the NaCl electrolyte, the experimental results on KCl highlight a salinity effect on the real part. According to the Debye theory, the real part of the complex permittivity should decrease with increment in salinity [1], [4], [20]. Based on the results published in [20], it can be observed that the real part of the dielectric constant of the KCl electrolyte is smaller than the one derived from measurements performed on NaCl assuming the same salinity and moisture content values. For instance, for $S = 100\%$ and $m_v = 30\%$, ϵ' decreases from 7.7 to 4.6 for KCl whereas ϵ' decreases from 17.5 to 12.5 for NaCl in the [2GHz – 7GHz] frequency range. Such a difference can be attributed to the solubility properties of salts. Actually, since the sylvite salt displays a higher solubility than halite, the amount of electronic charges resulting from the dissolution of KCl should then be greater than the one resulting from the dissolution of the same amount of NaCl salt: the higher is the solubility of a salt, and the greater is the amount of mobile ions in solution. As a result, the salinity effect resulting from the dissolution of KCl in a given water content should be higher than the effect derived from the dissolution of the same weight of NaCl in the same water content. Subsequently, assuming a salinity of $S = 100\%$ (which corresponds to 100g of salt dissolved in 1L of water), the real part of a KCl electrolyte should then be smaller than the one obtained on NaCl electrolyte, as observed in our experimental data sets which appear to be in good agreement with the Debye theory.

Nevertheless, some discrepancies in the real part could be observed between the laboratory and fieldwork measurements. Actually, compared to the real part derived from the KCl/NaCl water layer in Table II, the laboratory measurements revealed systematic higher values for the real part for the frequency range under consideration. Such differences can be attributed to both the mineralogical composition and the temperature effect. From the mineralogical point of view, the mixture of several saline species, as observed over Cottonball Basin, contributes to higher salinity values than the one considered for the laboratory experiments leading to an overestimation of the laboratory measurements since the real part has been shown to decrease with increment in salinity. Additionally, it is well known that the solubility properties of mineralogical species depend on the temperature. As an example, if the NaCl solubility slowly increases with the temperature (from 35.6g to 40.5g of anhydrous solute in 100g of solution in the [0°C – 100°C] temperature interval), the solubility of KCl increases from 27.6g to 58.3g in the same temperature range. Since the laboratory measurements have been performed at a temperature of $T=20^\circ\text{C}$, the solubility of KCl is

underestimated compared to the one occurring in Cottonball Basin where temperatures commonly exceed 50°C at the time of the fieldwork measurements. Such an underestimation in the solubility then results in smaller salinity values for the laboratory measurements contributing to higher real part of the dielectric constant of the sylvite electrolyte.

As the imaginary part is concerned, the measurement results are also in good agreement with the Debye-Falkenhagen theory as well as the frequency behavior of saline electrolytes reported in numerous papers ([1]-[2], [17]-[20], [37]), and the results derived from the Death Valley measurements. Actually, from **Figure 4**, it can be clearly observed that ϵ'' steeply decreases with incrementing frequency, especially for moisture contents exceeding the transition moisture, since the ionic conductivity is the main contributor of dielectric losses in the [1-4GHz] frequency range [15] [20], [23]. Since the ionic properties of salts are no more effective without free water component, the imaginary part is logically weaker for small water content as shown in **Figure 4**. As an example, for a moisture content below the transition moisture ($m_v < 20\%$), ϵ'' doesn't exceed 8 in the [1-7GHz] frequency range. On the contrary, an increment in water content leading to a greater concentration of mobile ions in solution, the effect of the frequency dependence of the ionic conductivity on the imaginary part becomes more effective. As mentioned above, the ionic conductivity increasing at low frequency, we logically observed a strong increase of the imaginary part at low frequency. As an example, ϵ'' increases up to 50 at L-band (2GHz) for water content exceeding 40% while ϵ'' decreases down to 15 at 7GHz.

Nevertheless some discrepancies for the frequency behavior occur for the real part of the dielectric constant in the [500MHz – 1.5GHz] frequency range where it can be observed that the real part presents an unexpected increase with frequency, especially when the water content exceeds the transition moisture value. However, this strong discrepancy can be explained by the blemishes due to the vectorial network analyzer which is not very relevant for very low frequencies (in the range [500MHz – 1GHz]). It should be noticed that for such reasons, the simulations of the radar backscattering coefficients by means of an IEM model presented in section V have been performed for frequencies higher than 1.5GHz.

IV. ANALYSIS OF AIRSAR AND SIR-C/X-SAR DATA

A. SIR-C/X-SAR and AIRSAR Data

In order to assess the influence of saline deposits in SAR imagery, two kinds of SAR images were considered in the following. The first data set is derived from the SIR-C/X-SAR

TABLE III

MEAN VALUE OF THE COPOLARIZED RATIO σ_{HH}/σ_{VV} EXTRACTED FROM SIR-C/X-SAR AND AIRSAR IMAGES FOR C-, L-, AND P-BAND. FOR EACH IMAGES THE COPOLARIZED RATIO IS AVERAGED OVER THE TEST SITE AREA INDICATED BY THE BLACK POLYGON IN FIGURE 5 WHICH CORRESPONDS TO THE HYPER-SALINE DEPOSITS UNDER CONSIDERATION.

SIR-C/X-SAR	σ_{HH}/σ_{VV}	Φ_{HHVV}	Frequency	Date of Flight
PR11317	0.31	22.7°	L-Band	04/16/1994
PR17825	0.34	23.8°	L-Band	04/16/1994
PR44392	0.44	10.5°	L-Band	09/30/1994
PR50315	0.43	11.5°	L-Band	09/30/1994
PR11318	0.25	11.8°	C-Band	04/16/1994
PR17826	0.26	11.1°	C-Band	04/16/1994
PR44393	0.51	6.9°	C-Band	09/30/1994
PR50316	0.51	7.2°	C-Band	09/30/1994

AIRSAR	σ_{HH}/σ_{VV}	Φ_{HHVV}	Frequency	Date of Flight
cm6507	0.14	13.1°	C-Band	04/10/1994
cm6838	0.14	14.6°	C-Band	04/10/1994
cm6507	0.27	28.8°	L-Band	04/10/1994
cm6838	0.26	29.9°	L-Band	04/10/1994
cm6507	0.17	7.8°	P-Band	04/10/1994

spaceborne system while the second one was obtained by means of the JPL/AIRSAR airborne sensor.

JPL/NASA Spaceborne Imaging Radar – C/ X-band Synthetic Aperture Radar (SIR-C/X-SAR) was an imaging radar that flew on two missions during 1994 (STS 59 and STS 68) onboard the Space Shuttle Endeavour. The both STS then provide us with temporal series of SAR images for the April and September-October 1994 periods. The SIR-C/X-SAR antenna structurally consisted of three individual antennas operating at different wavelengths: L-band (23.5 cm), C-band (5.8 cm), and X-band (3 cm). As L- and C-bands antennas are concerned, they were fully polarimetric allowing acquisitions in both horizontal (H) and vertical (V) polarizations, leading to 4 channels: 2 co-polarized (HH and VV) and 2 cross-polarized (HV and VH), while the X-band antenna operated at VV polarization only. Such a system then provided multi-frequency and multi-polarization radar images with a spatial resolution of 30 per 30 meters, not only in term of magnitude of the backscattering signal, but also in term of the relative phase difference, especially between the co-polarized channels allowing the derivation of the complete scattering matrix of a scene on a pixel by pixel basis. **Fig. 5** and **6** display images for both AIRSAR and SIR-C sensors, corresponding to the test site under consideration over the saltpan of Cottonball Basin located in Death Valley, CA. It should notice that the saltpan can be clearly observed.

Providing a better spatial resolution (12 x 12 meters), we also considered SAR images acquired the 10th of April 1994 with the JPL/NASA AIRSAR sensor. Similarly to SIR-C, the

AIRSAR system is a multi-frequency and fully polarimetric imaging radar. The cm6507 and cm6838 AIRSAR images were acquired at P-, L-, and C-bands (**cf. Fig. 5**) for all possible combinations of horizontal and vertical transmit and receive polarizations allowing the exploitation of both the amplitude and phase recorded in each pixel of the studied area.



Fig. 5: AIRSAR cm6507 image of the Death Valley displaying the total power recorded in the three frequencies: P-band (red), L-band (blue), and C-band (green). (Credit: NASA/JPL).

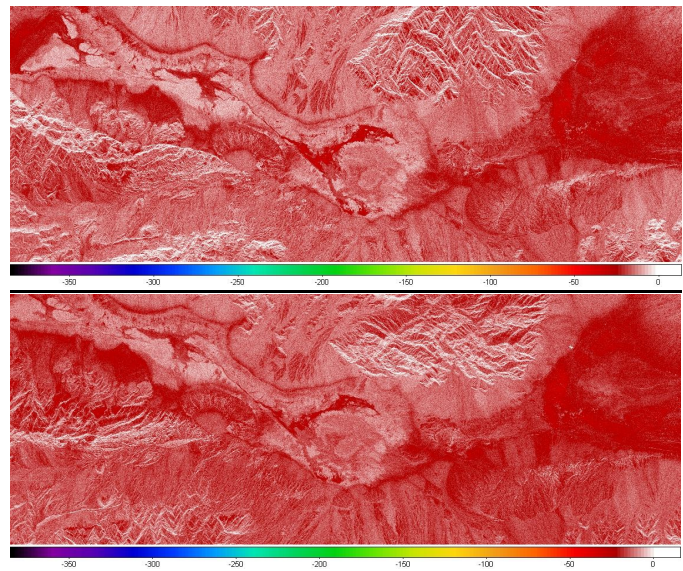


Fig. 6: Temporal series of L-Band SIR-C images of the Death Valley for HH polarization. The acquisition dates are the 16th of April (PR11317 on top) and the 30th of September (PR50315) 1994. The Cottonball Basin is clearly observed in the center of the images revealing a specific signature at the location of saline deposits (arrow) varying between the both acquisitions.

B. Analysis of the copolarized ratios derived from SIR-C/X-SAR and AIRSAR Data

Because of the specific dielectric properties of the saline deposits located in the Cottonball Basin test site, we expect such deposits to get a specific radar signature. According to recent works, it has been shown that the use of the radar copolarized ratio σ_{HH}/σ_{VV} is particularly suitable for assessing the complex dielectric constant of soils [27], [62]-[63] since such a ratio is theoretically independent of the surface roughness which isn't the case in experimental data related to rough surfaces [62]. Actually, including the second-order terms of the Small Perturbation Model (SPM), it has

been observed that such a ratio is affected by the roughness which the effect is to increase the copolarized ratio that is to make the $\nu\nu$ backscattering coefficient closer to that at hh polarization. Based on the single backscattering coefficients from the Integral Equation Model (IEM), [27] showed that the copolarized ratio is affected by the classical statistical roughness parameters (rms-height and correlation length) especially for high roughness conditions (rms-height $> 1.5\text{cm}$ and correlation length $> 10\text{cm}$ at L-band). Nevertheless, assuming small rms-height values (rms-height $< 1\text{cm}$), these authors showed that the copolar ratio is independent on the correlation length and weakly affected by the rms-height: the copolar ratio has shown to vary from less than 0.1dB at L-band for rms-height values $< 1\text{cm}$ and correlation length $< 10\text{cm}$ [27]. Thus, because of the small roughness parameters observed and measured over the saline deposits (rms-height = 0.3cm and correlation length = 2.7cm), we can consider that the independence of the copolarized ratio to the roughness as a first approximation is effective. In order to avoid possible effect of surface roughness, we then considered in the following the radar copolarized backscattering ratio derived from AIRSAR and SIR-C/X-SAR data which will further be compared to analytical IEM simulations presented in section V.

Based on the SIR-C/X-SAR and AIRSAR data, the analysis of the copolarized ratios of the radar backscattering coefficients revealed a typical $\sigma_{\text{HH}}/\sigma_{\text{VV}}$ signature all over the saltpan as it can be observed in **Figure 7**.

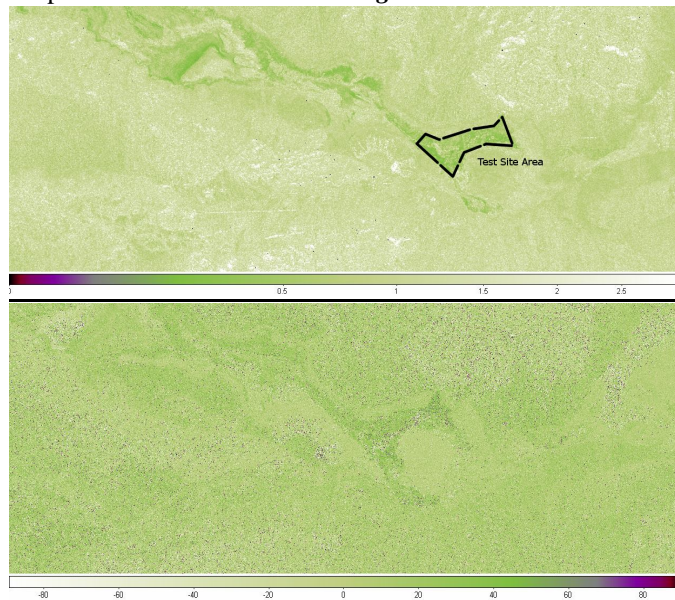


Fig. 7: Analysis of the copolarized backscattering ratio (on top) and phase difference (bottom) extracted from the SIR-C PR11317 acquisition. Typical $\sigma_{\text{HH}}/\sigma_{\text{VV}}$ and $\Phi_{\text{HH-VV}}$ signatures can be clearly observed and related to the presence of saline deposits over the Death Valley, especially for the test site under consideration delimited by the black polygon.

Table III summarizes the mean values of the copolarized ratio and copolar phase differences extracted from spaceborne and airborne SAR data after applying a smoothing window on

a 7×7 pixels basis. It should be pointed out that each $\sigma_{\text{HH}}/\sigma_{\text{VV}}$ ratio is averaged over the saltpan test site area corresponding to the black polygon displayed in Figure 7.

Providing us with temporal series, the copolar ratio listed in Table III suggest a seasonal effect related to the soil moisture content. Assuming the SIR-C/X-SAR data, it can be clearly observed that the copolarized ratio increases between the April and September acquisition dates, whatever the frequency may be. For instance, $\sigma_{\text{HH}}/\sigma_{\text{VV}}$ increases from 0.31-0.35 in April to 0.44 in September at L-band and from 0.25 to 0.51 at C-band. According to the yearly distribution of the precipitation recorded by official weather stations over the saltpan during the last 80 years, such an increase can be related to the weather and climatic conditions described in section II.B. Actually, following the wettest months (December, January, and February), the precipitation events lead to high soil moisture content combined to small roughness parameter: the highest is the moisture content of the crystal crust layer and the smoothest is the surface because the surface sodium chloride crust is dissolved by fresh water discharges. Such low roughness conditions being suitable for separating HH and VV behaviours, we logically observed the smallest copolarized ratios in April on both the SIR-C and AIRSAR data. On the contrary, following the hottest months (June, July, and August), the acquisitions performed at the end of September concern low soil moisture contents coupled to the desiccation of the crystal crust layer (in form of polygons of desiccation) leading to an increase in the surface roughness parameters. According to [27] and [62], such an increment in the roughness parameters should lead to an increase in the copolarized ratio since for rough surfaces the isotropic scattering distribution leads to the same HH and VV backscattering coefficients. As expected, $\sigma_{\text{HH}}/\sigma_{\text{VV}}$ presents a strong increase in September. The stronger increase observed for C-band compared to L-band can give some information concerning the roughness parameters since the roughness effect is more effective for parameters in the order of the wavelength. In summary, the variation in the copolarized ratio reflects the seasonal variation of the rainfall through the dependence of $\sigma_{\text{HH}}/\sigma_{\text{VV}}$ to the soil moisture content.

C. Analysis of the copolarized phase differences derived from SIR-C/X-SAR and AIRSAR Data

Dealing with the copolarized phase difference Φ_{HHVV} , we showed in previous studies that such a radar phase signal could be used as a moisture indicator [39], [64]. Since the expression of this phase signature is derived from the copolarized backscattering coefficients, the different behavior of the backscattering coefficients in each copolarized mode as revealed by the copolar ratio could then impact the phase signal. For that matter, we proceeded to the same analysis for

Φ_{HHVV} than the one performed for the copolar ratio. The copolar phase difference results reported in Table III represent the mean value of the Gaussian distribution of Φ_{HHVV} derived from the analysis of the test site area over the saltpan on a pixel basis.

From Table III, a strong correlation between the radar phase signal and the copolar ratio can be observed as well as a strong dependency to the seasonal data. For each frequency, Φ_{HHVV} appears to be inversely proportional to the copolarized ratio. As an example, assuming both the SIR-C/X-SAR and AIRSAR L-band data, the copolar phase signal decreases from 29.5° to 10.5° for an increment in $\sigma_{\text{HH}}/\sigma_{\text{VV}}$ from 0.26 to 0.44. The same observation may be done for C-band where the decrease of Φ_{HHVV} from 14.6 to 6.9 corresponds to an increase of $\sigma_{\text{HH}}/\sigma_{\text{VV}}$ from 0.14 to 0.51. Based on the temporal series, the variations in the copolarized phase difference show a correlation with the acquisition date and then with the weather and climatic conditions. Such a variation support the assumption of [39] and [64], that the copolar phase signal is related to the moisture content of soils: the highest is the soil water content, and the highest is the radar phase signal. For instance at L-band, Φ_{HHVV} increases from 10° - 11° in September (corresponding to the lowest soil moisture conditions) to 23° - 30° in April (corresponding to the highest soil water content). In the same way, Φ_{HHVV} increases from 7° in September to 15° in April at C-band.

Such a correlation of Φ_{HHVV} with the copolarized ratio as well as the seasonal behavior can be predicted on the basis of the analytical expression of the copolarized phase difference given in [39] and [64]. Assuming the single surface scattering term only, the copolarized phase difference depends on the difference between the copolarized backscattering coefficients. An increase in the difference between σ_{hh} and σ_{vv} then results in an increase in the copolar phase signal. Since in April, the weather and climatic conditions lead to highly smoothed and moistened surfaces suitable for separating HH and VV behaviours, we expect to have the highest copolar phase differences correlated to smallest copolarized ratios. On the contrary, because of the surface crystal layer desiccation following the driest and hottest months, the surface roughness and soil moisture conditions make the vv backscattering coefficient closer to that at hh polarization because of the occurrence of the isotropic scattering distribution. Following to that, the copolarized ratio is expected to increase in September while the copolarized phase difference should decrease. As expected, the copolarized ratios and phase differences extracted from airborne and spaceborne SAR data display such a behavior.

V. COMPARISON OF SAR DATA WITH THE IEM MODELING OF THE COPOLARIZED BACKSCATTERING RATIOS AND PHASE DIFFERENCES

In order to confirm the dielectric properties of saline deposits to be responsible of the particular copolarized backscattering ratios and phase differences observed on both airborne and spaceborne SAR images, we now consider an analytical approach based on IEM simulations of the copolarized backscattering ratios for the AIRSAR and SIR-C parameters (in terms of incidence angle, polarization, wavelength) as well as the roughness parameters observed over the saltpan.

Because of the small roughness parameters recorded on the moistened saline deposits observed over the saltpan, the analytical simulations of the copolarized ratio were performed by means of the single backscattering coefficients derived from the IEM surface scattering model since the single scattering will dominate over the multiple scattering. The IEM single backscattering coefficients are given by [24]:

$$\sigma_{SSpp}^0(\theta) = \frac{k}{4} e^{-2k^2 \cos^2(\theta)\sigma^2} \sum_{n=1}^{\infty} |I_{pp}^n|^2 \frac{W^{(n)}(2k \sin(\theta))}{n!} \quad (6)$$

with:

$$I_{pp}^n = (2k \cos(\theta)\sigma)^n f_{pp} e^{-k^2 \cos^2(\theta)\sigma^2} + \frac{(k \cos(\theta)\sigma)^n}{2} * [F_{pp}(-k \sin(\theta)) + F_{pp}(k \sin(\theta))] \quad (7)$$

and:

$$W^{(n)}(-2k \sin(\theta)) = \sqrt{\frac{\pi}{n}} L e^{-\frac{(kL \sin(\theta))^2}{n}} \quad (8)$$

where pp denotes the polarization state of the emitted/scattered wave respectively (HH or VV), θ is the incident angle, k the wavenumber, W^n the Fourier transform of the n th power of the surface correlation function assumed to be Gaussian described by means of the classical statistical roughness parameters namely the rms-height σ and the correlation length L .

It should be pointed out that [27] found a good agreement between the IEM single-scattering model and the L-band measurements of SIR-C and AIRSAR over a well managed watershed in southwest Oklahoma (Little Washita River) for a wide range of soil moisture and surface roughness conditions. Such an agreement for L-Band AIRSAR data accounts for the choice of the IEM model for the following theoretical analyses of the copolarized ratios.

The simulation will first aim at defining whether the single-scattering IEM model can reproduce the copolarized backscattering ratios derived from C- and L-Band SAR data. Afterwards, by directly relating and comparing SAR measurements to theoretical model predictions, we will propose the use of the copolarized radiometric and phasimetric signal as indicators of moistened saline deposits, not only in order to infer an estimation of the soil moisture and the dielectric properties of the hyper-saline areas, but also

to follow the seasonal variations of such properties.

A. Analysis of the copolarized backscattering ratio derived from IEM analytical simulations

IEM simulation results are presented in **Fig. 8** according to the SIR-C/X-SAR and AIRSAR sensor parameters. As the roughness parameters are concerned, we considered the values of rms-height and correlation length observed during the fieldwork campaign, that is $\sigma = 0.3\text{cm}$ and $L_c = 3\text{cm}$. Since the IEM model requires the knowledge of the complex permittivity of soils, we assumed the dielectric constant values derived from the measurements performed over the saltpan as a reasonable approximation of the dielectric input parameters. Because of the frequency limitations of the laboratory measurements induced by the vectorial network analyzer, the input frequencies for the IEM simulations are set at 1.5GHz for L-band (whereas the L-band frequency is about 1.26GHz for the both SAR systems) and 5.3GHz for C-band. The incidence angles are derived from the near look and far look angles related to each SAR image. By identifying the pixel location of the saltpan on each image, the input incidence angles were set at 44° for SIR-C/X-SAR images and 59° for the AIRSAR ones.

Moreover two cases have been investigated to reflect the variations of the soil moisture conditions corresponding to both April (wet case) and September (dry case) acquisition dates: the dielectric constant for April simulations derives from the fieldwork measurements while the ones for September are based on laboratory measurements performed on NaCl and KCl electrolytes.

From **Fig. 8**, two behaviours of the copolar ratio can be clearly observed. The first one relates to the dependence of the ratio to the moisture content of soils while the second one concerns the impact of salinity on the copolarized ratio. Actually, assuming both C-, and L-band frequencies, **Fig. 8** indicates that the copolarized ratio decreases with increment in the dielectric constant that is with increment in soil moisture content: the higher is the moisture content, the higher is complex permittivity, and the smaller is the copolarized backscattering ratio. As an example, according to the L-Band SIR-C simulations, $\sigma_{\text{HH}}/\sigma_{\text{VV}}$ decreases from 0.53 to 0.29 for increasing complex permittivity from 3.5-3.5j to 10-50j. The same observation holds for the AIRSAR simulations with a decrease of $\sigma_{\text{HH}}/\sigma_{\text{VV}}$ from 0.63 to 0.23 for the same permittivity range. Changing the frequency to C-band, the IEM simulations predict a variation of the copolarized ratio from 0.43 to 0.24 for an increment in the dielectric constant from $\epsilon = 3.5 - 3.5j$ to $\epsilon = 8 - 13j$. Such a variation of the copolarized ratio can be explained by means of the physical based explanations described in the previous sections. Assuming high soil moisture contents combined with small roughness parameters leads to perfectly reflective

surfaces suitable for separating the vertically polarized backscattering coefficient from the horizontally polarized mode [2], [24], [27], and [62]. It results in a decrease of the backscattering copolarized ratio.

If the increment in the roughness parameters associated to the desiccation phenomenon is expected to slightly impact the L-band (because of roughness parameters smaller to the $\lambda = 23\text{cm}$ wavelength), we nevertheless have to assess the impact of increment in roughness parameters leading to parameters comparable to the wavelength at C-band ($\lambda = 6\text{cm}$). By fixing the values of the rms-height and the correlation length to 0.8cm and 5cm respectively (**Fig. 8** bottom right), the IEM simulation results predict a decrease from 0.61 to 0.35 for an increment in permittivity from $\epsilon = 3.5 - 3.5j$ to $\epsilon = 8 - 13j$. Such an increment of the copolarized ratio is in good agreement with the dependency of the copolarized ratio reported in [27], and supports the assumption that an increment in the roughness parameters should lead to an increase in the copolarized ratio since for rough surfaces the isotropic scattering distribution leads to the same HH and VV backscattering coefficients.

Another interesting result concerns the copolarized ratio dependence on the salinity through the imaginary part of the complex permittivity, especially at L-band. As shown in **Fig. 8**, the L-band copolarized backscattering ratio appears to slowly vary with the real part of the dielectric constant. On the contrary, the ratio displays a strong dependence to the imaginary part whatever the real part may be. As an example, by fixing the real part to $\epsilon' = 6$, $\sigma_{\text{HH}}/\sigma_{\text{VV}}$ decreases from 0.5 to 0.27 for the SIR-C simulations at L-band and from 0.60 to 0.21 for the AIRSAR simulations over an increment of the imaginary part from $\epsilon'' = 3$ to 68. Such a dependence of the copolarized ratio to the imaginary part lies in the ionic conductivity which reflects the salinity effect. As mentioned in [20], the vertically polarized backscattering coefficient is more sensitive to the salinity than the horizontally polarized one. The difference between σ_{VV}^0 and σ_{HH}^0 increases with the soil moisture content and then the salinity since an increment in soil water content leads to a higher free water component allowing the occurrence of greater amounts of mobile ions in solution. It results in a copolarized ratio inversely proportional to the imaginary part of the dielectric constant that is to the salinity. To summarize, at L-band the dependence of the radar ratio to the imaginary part dominates over the dependence on the real part as observed on **Fig. 8** for both AIRSAR and SIR-C IEM simulations. On the contrary, since the ionic conductivity has shown to be inversely proportional to the frequency [20]-[23], an increment in frequency from L- to C-band results in a decrease of the imaginary part as displayed in the laboratory measurement section (section III + [20]). Under these assumptions, the effect of salinity on the copolarized ratio should then be reduced leading to equal contributions of the real and imaginary parts on the copolarized ratio. The IEM

simulations results performed at C-band confirm such a hypothesis by displaying the same variation of the copolarized ratio with increment according to both real and imaginary parts (in the form of concentric lines observed in *Fig. 8*). For instance at C-band (*Fig. 8* bottom left), $\sigma_{\text{HH}}/\sigma_{\text{VV}}$ decreases from 0.45 to 0.3 for an increase of the real part from 3.5 to 10 while the same variation of the ratio holds for an increase of the imaginary part from 3.5 to 8.

Such results suggest that L-band should be more relevant for the detection and mapping of moistened and hyper-saline deposits and to follow the seasonal variations of their dielectric properties because of the steep increase of the imaginary part at low frequency compared to the real part. On the contrary, C-band should be more suitable for the detection and mapping of seasonal variations of soil moisture only since the imaginary part strongly decrease with increment in frequency (section III+[20]).

B. Analysis of the copolarized phase difference derived from IEM analytical simulations

Fig. 9 illustrates the IEM simulations of the copolarized phase difference Φ_{HHVV} performed at L- and C-band. The analytical simulations have been realised by means of the analytical expression of the copolarized phase difference given in [64] neglecting the multiple scattering as well as the subsurface scattering terms. Under these circumstances, Φ_{HHVV} is a function of the difference between the surface backscattering coefficients in each copolarized mode. In particular, the copolarized phase difference has shown to be inversely proportional to the copolarized ratio since Φ_{HHVV} increases with increment in the difference between the copolarized backscattering coefficients. From *Fig. 9*, such a dependence can be clearly observed for the frequency bands under consideration. For instance, the L-band IEM simulations of the copolarized phase difference predict an increase from about 7° to 31° for SIR-C parameters and 4° to 35° for the AIRSAR parameters when considering an increment of the complex permittivity from $\epsilon = 3.5 - 3.5j$ to $\epsilon = 10 - 50j$. Such variations correspond to a decrease of the copolarized ratio from 0.53 to 0.29 according to SIR-C parameters and from 0.63 to 0.23 for the AIRSAR ones. By changing the frequency from L- to C-band, the same tendency with respect to the complex permittivity can be observed. Assuming a variation of the dielectric constant from $\epsilon = 3.5 - 3.5j$ to $8 - 13j$, the IEM simulations predict an increment in Φ_{HHVV} from 4° to 18° corresponding to a decrease of $\sigma_{\text{HH}}/\sigma_{\text{VV}}$ from 0.43 to 0.24.

It should be noticed that Φ_{HHVV} reflects the same dependency on the salinity and moisture than the one observed for the copolar ratio since the analytical expression of the phase signal leads to linear variations of the phase signal with the copolar ratio. Actually, it can be seen that

Φ_{HHVV} slightly increases with increment in the real part of the dielectric constant whereas the simulation results suggest stronger variations with respect to the imaginary part at L-band. For instance, considering a real part set at $\epsilon' = 6$, the simulation results predict an increase in Φ_{HHVV} from 9° to 32° according to an increment of the imaginary part from $\epsilon'' = 3$ to 68 corresponding to a variation of $\sigma_{\text{HH}}/\sigma_{\text{VV}}$ from 0.53 to 0.28. On the contrary, because of the lower values of the imaginary part at C-band (due to the frequency dependence of the ionic conductivity as previously mentioned), Φ_{HHVV} appears to be dependent on both the real and imaginary parts of the dielectric constant.

C. Comparison to the copolarized ratios and phase differences extracted from SIR-C/X-SAR and AIRSAR data.

In this section, we compare the values generated by the single scattering IEM model with those derived directly from the L-, and C-band SIR-C and AIRSAR images on the days listed in Table III. All the measured and generated copolarized ratios are reported in *Fig. 10*.

As the copolarized ratio is concerned, the IEM simulation results provide good agreement with the values extracted from SAR images especially at L-band. According to the L-band SIR-C data, the seasonal variations of $\sigma_{\text{HH}}/\sigma_{\text{VV}}$ between the April and September acquisition dates can be easily reproduced. Assuming the L-band dielectric properties of the dry NaCl layer measured over the saltpan as representative of the dielectric properties occurring during the driest period (corresponding to the September acquisition date), the IEM simulations predicts a copolar ratio in the range 0.39-0.42 according to the SIR-C parameters and 0.38-0.43 for the AIRSAR ones, while the SIR-C/X-SAR data give 0.43 and 0.44 in September 1994. Considering the April acquisition date, we assume an intermediate complex dielectric constant for L-band of $\epsilon = 9 - 45j$ in order to take into account the both contributions of the wet NaCl surface layer and Wet Clay layer occurring during the wet period (namely the April acquisition date) as observed at the time of our fieldwork measurements in April 2007. Under these assumptions, the IEM simulations predict a copolarized ratio of about 0.3 according to SIR-C parameters and 0.23-0.24 for AIRSAR parameters. As it can be seen from *Fig. 10*, these results are in good agreement with the ones derived from the SAR data displaying a copolarized ratio of $\sigma_{\text{HH}}/\sigma_{\text{VV}} = 0.31$ -0.34 and 0.26-0.27 for SIR-C and AIRSAR respectively.

Changing the frequency from L- to C-band, the IEM simulations once again provide good estimates for the copolarized ratio. Based on the complex permittivity measurements performed on Death Valley at C-band, we assumed the following dielectric constants of $\epsilon = 3.2 - 3.7j$ and $\epsilon = 7.5 - 12j$ as representative for the September (dry case) and April (wet case) acquisition dates respectively.

Under these circumstances, the IEM simulations display a copolarized ratio of about 0.25 for April, while the C-band SIR-C data give 0.25 and 0.26 for the same period. Nevertheless some discrepancies appear when considering the AIRSAR result as observed in **Fig. 10**. Actually, the ratio derived from the AIRSAR data indicates a smaller copolarized ratio of 0.14. According to the IEM simulations, such a ratio suggests higher soil moisture content leading to higher dielectric properties than the one expected maybe due to rainfall events at the time or right before the AIRSAR acquisitions compared to the SIR-C acquisitions performed one week later. Such higher dielectric conditions could also account for the smaller ratio observed at L-band between the SIR-C (0.31-0.34) and AIRSAR (0.26-0.27) data since the copolarized ratio has shown to decrease with increment in the complex permittivity. Another discrepancy concerns the September acquisition date for which the SIR-C/X-SAR data analysis reveals a copolarized ratio of 0.51 whereas the IEM simulations predict a smaller ratio of about 0.41-0.42. These smaller values can be explained by the roughness effect induced by the desiccation phenomenon. Indeed, taking into account higher roughness conditions derived from observations performed on polygons of desiccation, the IEM simulation results lead to fairly good estimates of the copolarized ratio closed to 0.56 (cf. **Fig. 10**).

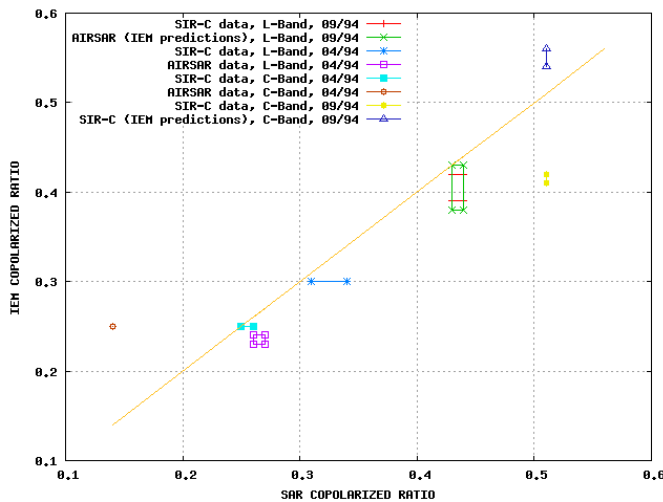


Fig. 10: Comparison of the copolarized ratio values generated by the single scattering IEM model with those derived directly from the L-, and C-band SIR-C/X-SAR and AIRSAR images on the days listed in Table II. Good agreement between SAR and IEM ratios can be observed especially at L-band. The seasonal variation of the copolarized ratio can be also clearly observed.

Considering the assumptions previously formulated for the input dielectric parameters, we compared the copolarized phase difference values generated from the analytical scattering model with those extracted from the SAR data. For ease of reference, comparisons are reported in **Fig. 11**. Compared to the L-band data, the IEM simulations allow to correlate the variations of Φ_{HHVV} to the seasonal variations of the dielectric properties due to changes in soil moisture content between April and September. Moreover these

changes in the copolarized phase difference agree well with the ones observed on SAR images. As an example, the simulated phase indicates an increase from about 10° - 13° to 32° - 34° between September and April, when considering the AIRSAR parameters while the AIRSAR cm6507 and cm6838 data reveal a phase signal in the range 28.8° - 29.9° in April 1994. As the SIR-C parameters are concerned, the IEM simulations predict an increase of about 13° - 16° between September and April (from 14° - 17° in September to 30° in April) whereas the SIR-C/X-SAR data give an increment of the phase signal of about 11° - 13° (from 10.5° - 11.5° in September to 22.7° - 23.8° in April). It should be noticed that even if the simulated phase according to SIR-C parameters seems to be overestimated (maybe because of the calibration of the SAR system which isn't taken into account in the IEM modelling work), the absolute seasonal variation agrees well between L-band SAR data and IEM results.

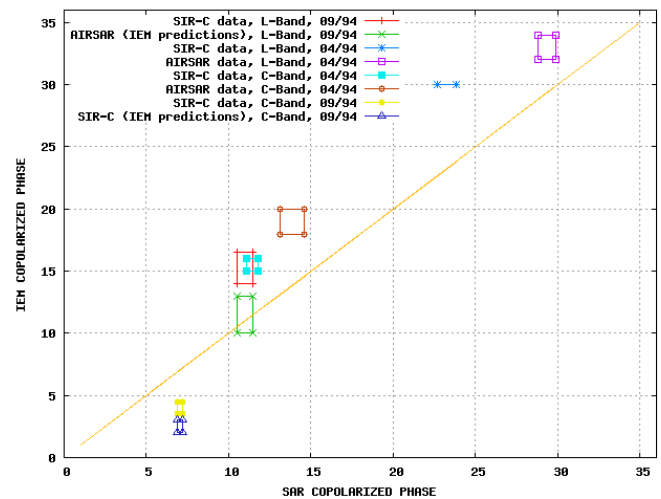


Fig. 11: Comparison of the copolarized phase differences values generated by the single scattering IEM model with those derived directly from the L-, and C-band SIR-C/X-SAR and AIRSAR images on the days listed in Table II. If good agreement between SAR and IEM phase differences can be observed at L-band, some discrepancies appear according to C-band.

On the contrary, the simulation results at C-band indicate some discrepancies in the estimation of the copolarized phase signal. For instance, considering the SIR-C parameters, the simulated phase presents an increase from 3.5° - 4.5° to 15° - 16° between September and April while the SIR-C data show an increase from 6.9° - 7.2° to 11.1° - 11.8° . The same observations holds for AIRSAR for which the simulated result tends to overestimate the phase signal extracted from AIRSAR images: the IEM Φ_{HHVV} is in the range 18° - 20° whereas the copolarized phase difference derived from AIRSAR data doesn't exceed 13.1° to 14.6° . Moreover, taken into account the roughness effect for SIR-C simulations due to the increase in the roughness parameters expected in September because of the desiccation, the simulated copolarized phase difference logically decreases to 2° - 3° since the difference between the copolarized backscattering coefficients decreases. Under these assumptions the absolute

simulated phase increment is in the range 15° - 18° while the copolar phase difference extracted from SIR-C data reveal an increase of 5° only between September and April 1994. Nevertheless, the underestimation observed in September between the simulated and SAR phase difference can be due to the multiple scattering terms [64]-[65]. Actually, previous studies [64] showed that the copolarized phase difference should increase with increment of roughness parameters of wet interfaces (the moisture profile can be regarded as a roughness profile) because of the multiple scattering occurring at the wet interface. Assuming the desiccation effect that should occur in September, the single surface scattering model would not be sufficient to reproduce the phase difference since the geometry should consider a rough and dry NaCl crust layer covering a wet Clay layer. Under these assumptions, we can expect the occurrence of air voids between the NaCl crust and Clay layers leading to multiple scattering. As demonstrated in [64], such multiple scattering will contribute to depolarize the incident wave leading to an additional phase difference term. According to the roughness parameters dimensions, the multiple scattering have then to be taken into account for the C-band simulations and should result in an increase of the copolar phase signal in September as observed on SIR-C/X-SAR data.

VI. DISCUSSION AND CONCLUSION

If it is well known that moisture influences the dielectric properties of natural media, the occurrence of salts will also affect the microwave dielectric properties of soils. Because of the dependence of the imaginary part of the complex permittivity on the ionic conductivity induced by the presence of saline minerals, we showed that SAR systems could be of great interest in the detection and mapping not only of soil moisture, but also of hyper-saline deposits.

Based on temporal AIRSAR and SIR-C/SAR series acquired over the saltpan of Death Valley (CA), as well as on electromagnetic characterization and analytical IEM simulations, we highlighted the abilities of SAR system to follow seasonal variations of soil moisture (through the variation in the dielectric properties). More especially, assuming the complex dielectric constants derived from laboratory and fieldwork measurements performed on Cottonball Basin as input parameters of the IEM scattering model, the analytical simulations allowed to reproduce the seasonal variations of both the copolarized backscattering ratios and phase differences observed on SAR images, and correlated to the saline deposits. The IEM simulations also allowed relating these specific copolarized signals to the seasonal variations of the complex permittivity of soils according to the dependence of the copolar ratio and phase difference on both the moisture and salinity observed on SAR images, and correlated to the saline deposits.

Compared to the analysis of airborne and spaceborne SAR data, our IEM simulation results indicate that the copolarized ratio decreases with increment in the dielectric constant that is with increment in soil moisture content: the higher is the moisture content, the higher is complex permittivity, and the smaller is the copolarized backscattering ratio. The copolarized ratio has also shown to be salinity dependent because of the imaginary part of the complex permittivity, especially at L-band. Actually, both SAR data and analytical results indicate that the copolarized ratio slowly vary with the real part of the dielectric constant whereas it displays a strong dependence to the imaginary part whatever the real part may be. To summarize, the copolarized ratio appears to be inversely proportional to the imaginary part of the dielectric constant that is to the salinity, especially for L-band.

The IEM simulation results confirmed that such a behavior lies in the difference between σ_{VV}^O and σ_{HH}^O which increases with the soil moisture content and then the salinity since an increment in soil water content leads to a higher free water component allowing the occurrence of greater amounts of mobile ions in solution. In other words, the salinity appears to be the main contributor in the variations of the copolarized ratio and phase difference because of the strong impact of the ionic conductivity on the imaginary part of the complex permittivity, especially at L-band which displays high variations of the imaginary parts. Because of the frequency dependence of the ionic conductivity, the salinity effect on the copolarized signals decreases at C-band for which the roughness should be included in order to account for the desiccation effect occurring during the dry season.

Because of the relation existing between the copolarized ratio and the copolarized phase difference, we showed that the dependence on moisture and salinity observed for the ratio holds for the radar phase signal. In particular, the phase signal extracted from SAR images as well as the simulated phase display good agreement according to seasonal variations. Our results indicate that Φ_{HHVV} slightly increases with increment in the real part of the dielectric constant whereas Φ_{HHVV} displays stronger variations with respect to the imaginary part at L-band. On the contrary, because of the lower values of the imaginary part observed at C-band (due to the frequency dependence of the ionic conductivity as previously mentioned), Φ_{HHVV} appears to be dependent on both the real and imaginary parts of the dielectric constant.

It should also be pointed out that even if the IEM simulations seem to slightly underestimate the values extracted from SAR data because of the lack of knowledge concerning the precise dielectric and roughness parameters at the time of the SAR acquisitions, they nevertheless provide a fairly good estimation of the copolarized ratios and phase differences observed on SAR images. These analytical simulations also allow confidently relating the variation in the copolarized ratio and phase signals to the seasonal variations of the dielectric properties of the hyper-saline

deposits. As the C-band is concerned, we also investigated the roughness effect on the copolar ratios and phases since the desiccation effect should induced increment of surface roughness parameters. For that matter, further studies will include the multiple scattering component in the computation of the copolarized phase difference since it has been shown that the multiple scattering impact the copolarized phase difference of moistened soils. Such a multiple scattering component is expected to be responsible of the discrepancies observed at C-band between the results derived from SAR data and the IEM simulation results.

Our results also suggest that L-band should be more relevant for the detection and mapping of moistened and hyper-saline deposits and to follow the seasonal variations of their dielectric properties because of the steep increase of the imaginary part at low frequency compared to the real part. On the contrary, C-band should be more suitable for the detection and mapping of seasonal variations of soil moisture only since the imaginary part strongly decrease with increment in frequency.

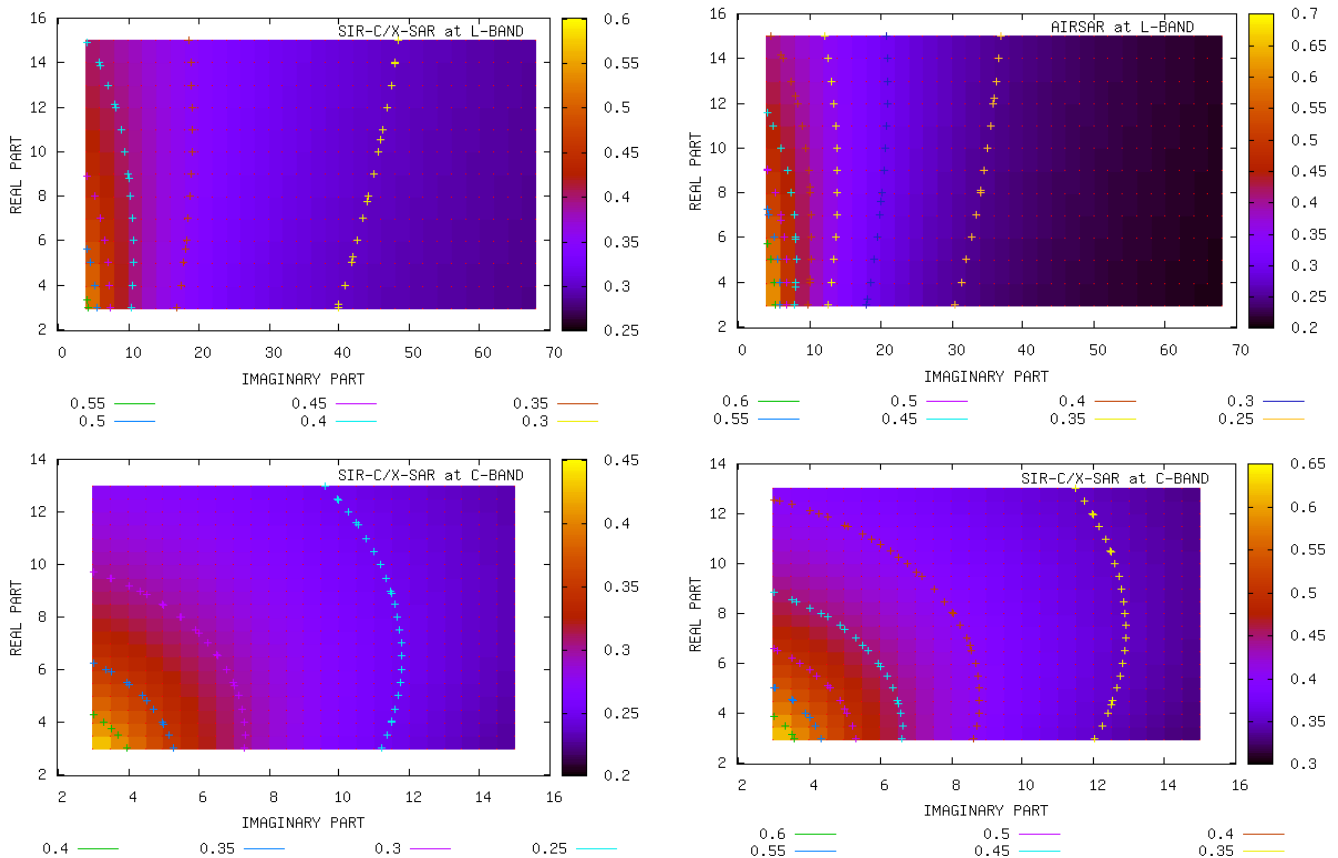


Fig. 8: IEM simulations of the copolarized backscattering ratios as function of the real and imaginary parts of the complex permittivity enclosing the extreme values derived from fieldwork measurements conducted over the saltpan in April 2007. The copolar ratios are computed according to the SIR-C/X-SAR and AIRSAR acquisition parameters in terms of incidence angle (set at $\theta_i = 44^\circ$ for SIR-C/X-SAR and 59° for AIRSAR), and frequency (1.5GHz for L-band and 5.3 GHz for C-band). The input roughness parameters are derived from fieldwork measurements (top + bottom left). In order to take into account the desiccation effect expected in September, additional IEM simulations were performed at C-band assuming an increment in the roughness parameters (bottom right). The moisture and salinity dependence of the copolarized ratio can be clearly observed.

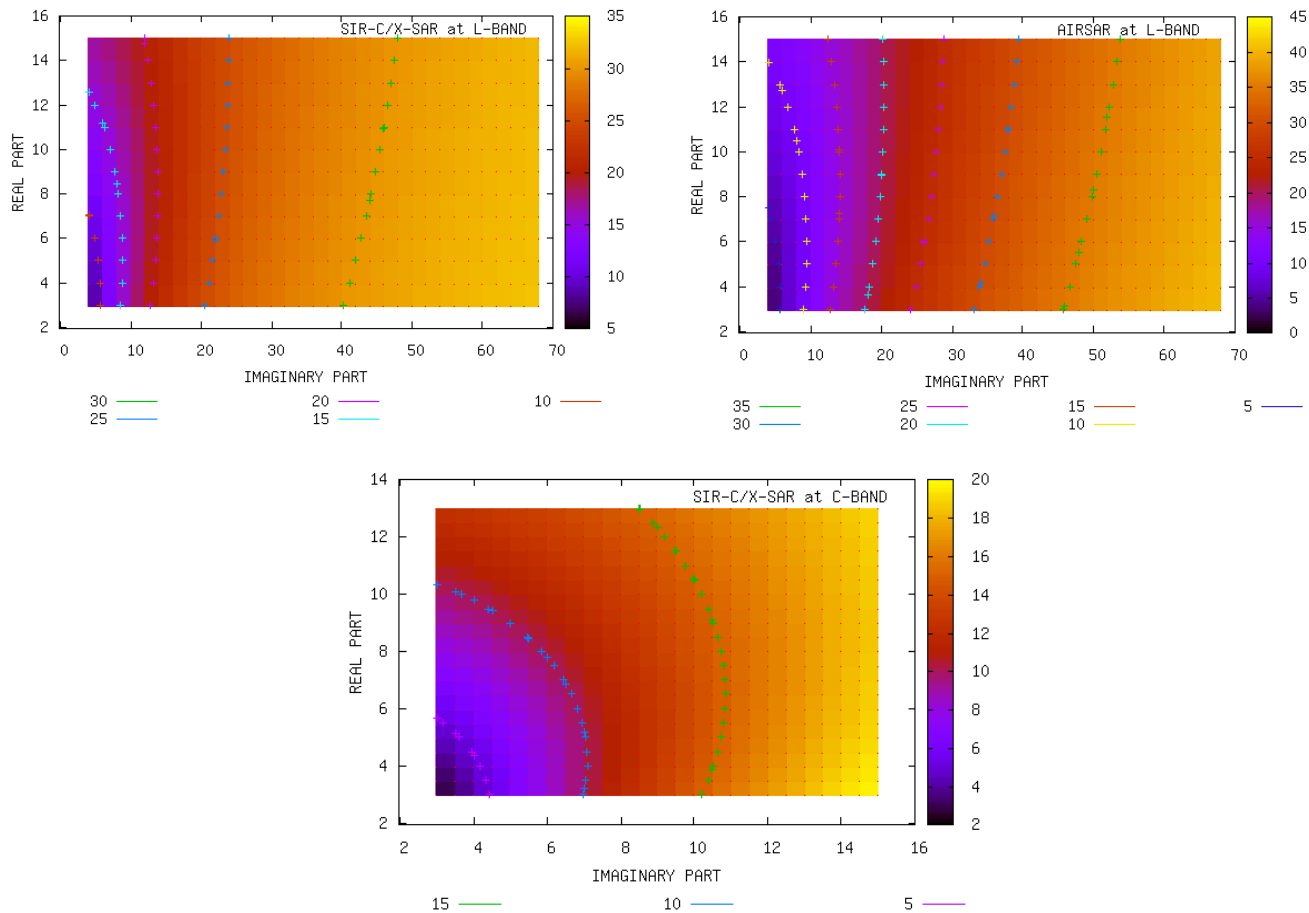


Fig. 9: IEM simulations of the copolarized phase differences as function of the real and imaginary parts of the complex permittivity enclosing the extreme values derived from fieldwork measurements conducted over the saltpan in April 2007. The copolar phase differences are computed according to the SIR-C/X-SAR and AIRSAR acquisition parameters in terms of incidence angle (set at $\theta_i = 44^\circ$ for SIR-C/X-SAR and 59° for AIRSAR), and frequency (1.5GHz for L-band and 5.3 GHz for C-band). The input roughness parameters are derived from fieldwork measurements.

REFERENCES

[1] J. R. Wang, and T. J. Schmugge, "An empirical model for the complex dielectric permittivity of soils as a function of water content," *IEEE TGRS*, vol. GE-18, pp. 288-295, 1980.

[2] F. T. Ulaby, R. K. Moore, and A. K. Fung, *Microwave Remote Sensing: Active and Passive*, Norwood, MA: Artech House, Appendix E, pp. 2017-2119, 1981.

[3] A. M. Shutko and E. M. Reutov, "Mixture formulas applied in estimation of dielectric and radiative characteristics of soils and grounds at microwave frequencies," *IEEE TGRS*, vol. GE-20, no. 1, pp. 29-32, 1982.

[4] M. Hallikainen, F. T. Ulaby, M. C. Dobson, M. A. El-Rayes, and L. K. Wu, "Microwave dielectric behavior of wet soil - Part I: empirical models and experimental observations," *IEEE TGRS*, vol. GE-23, pp. 25-34, 1985.

[5] M. C. Dobson, F. T. Ulaby, M. T. Hallikainen, and M. A. El-Rayes, "Microwave dielectric behavior of wet soil - Part II: Dielectric mixing models," *IEEE TGRS*, vol. GE-23, pp. 35-46, 1985.

[6] V. L. Mironov, S. A. Komarov, N. V. Rychkova, and V. N. Kleshchenko, "Study of dielectric properties of wet grounds at microwave frequencies," *Earth Obs. Rem. Sens.*, vol. 12, pp. 495-504, 1995.

[7] N. R. Peplinsky, F. T. Ulaby, and M. C. Dobson, "Dielectric properties of soils in the 0.3-1.3 GHz range," *IEEE TGRS*, vol. 33, pp. 803-807, 1995.

[8] D. A. Boyarskii, V. V. Tikhonov, and N. Yu. Komarova, "Model of dielectric constant of bound water in soil for applications of microwave remote sensing," *Progress in Electromagnetics Research, PIER* 35, pp. 251-269, 2002.

[9] J. A. Lane, and J. A. Saxton, "Dielectric dispersion in pure polar liquids at very high radio frequencies. III. The effect of electrolytes in solution," *Proc. Roy. Soc.*, vol. 213, pp. 531-545, 1952.

[10] P. Weyl, "On the change in electrical conductance of sea water with temperature," *Limnol. Oceanogr.*, vol. 9, pp. 75-78, 1964.

[11] R. Cox, J. Riley, and G. Skirrow, "The physical properties of sea water," *Chem. Oceanogr.*, vol. 3, New York: Academic Press, 1965.

[12] A. Stogryn, "Equations for calculating the dielectric constant of saline water," *IEEE TMTT*, pp.733-736, 1971.

[13] K. R. Carver, "Microwave remote sensing of saline seeps," *Proceedings of Microwave Remote Sensing Symposium* (Houston, TX: NASA Johnson Space Center), pp. 216-231, 1977.

[14] K. Sreenivas, L. Venkataraknam, and P. V. Narasimha Rao, "Dielectric properties of salt-affected soils," *Int. J. Remote Sens.*, vol. 16, pp. 641-649, 1995.

[15] J. Sabburg, J. A. R. Ball, and N. H. Hancock, "Dielectric behavior of moist swelling clay soils at microwave frequencies," *IEEE TGRS*, vol. 35, pp. 784-787, 1997.

[16] V. L. Mironov, S. A. Komarov, and V. N. Kleshchenko, "Effect of salinity on the dielectric properties of wet earth at positive and negative temperatures," *Earth Obs. Rem. Sens.*, vol 15, pp. 221-231, 1998.

[17] S. A. Komarov, V. L. Mironov, and A. N. Romanov, "Frequency dispersion in microwave for complex permittivity of bound water stored in soils and wet salts," *IGARSS'99*, vol. 5, pp. 2643-2645, 1999.

[18] Q. Hu, Y. Shao, and H. Guo, "Microwave dielectric behavior of moist salt soil - Experimental observations and improve dielectric models," *Proceedings of IGARSS 2003*.

[19] V. L. Mironov, M. C. Dobson, V. H. Kaupp, S. A. Komarov, and V. N. Kleshchenko, "Generalized refractive mixing dielectric model for moist soils," *IEEE TGRS*, vol. 42, pp. 773-785, 2004.

[20] Y. Lasne, Ph. Paillou, A. Freeman, T. Farr, K. McDonald, G. Ruffié, J.-M. Malézieux, B. Chapman, and F. Demontoux, "Effect of salinity on the dielectric properties of geological materials: Implication for soil moisture

- detection by means of radar remote sensing," *IEEE TGRS*, vol. XX, pp. XX-XX, 2008.
- [21] J. B. Hasted, D. M. Ritson, and C. H. Collie, "Dielectric properties of aqueous ionic solutions. Parts I and II," *J. Chem. Phys.*, vol. 16, pp. 1-21, 1948.
- [22] H. Falkenhagen, "The principal ideas in the interionic attraction theory of strong electrolytes," *Reviews of Modern Physics*, vol. 3, pp. 412-426, 1931.
- [23] A. Chandra, and B. Bagchi, "Frequency dependence of ionic conductivity of electrolyte solutions," *Journal of Chemical Physics*, vol. 112, pp. 1876-1886, 2000.
- [24] A.K. Fung, *Microwave Scattering and Emissions Models and Their Applications*, Norwood, MA: Artech House, 1994.
- [25] L. Tsang, J. A. Kong, and R. T. Shin, *Theory of Microwave Remote Sensing*, New York: Wiley, 1985.
- [26] R. Bindlish, and A. P. Barros, "Subpixel variability on remotely sensed soil moisture: An inter-comparison study of SAR and ESTAR," *IEEE TGRS*, vol. 40, pp. 326-337, 2002.
- [27] J. Shi, J. Wang, A. Y. Hsu, P. E. O'Neill, and E. T. Engman, "Estimation of bare surface soil moisture and surface roughness parameter using L-Band SAR image data," *IEEE TGRS*, vol. 35, pp. 1254-1266, 1997.
- [28] F. T. Ulaby, P. P. Batlivala, and M. C. Dobson, "Microwave backscatter dependence on surface roughness, soil moisture, and soil texture, Part I - Bare soil," *IEEE TGE*, vol. GE-16, pp. 286-295, 1978.
- [29] P. Dubois, J. van Zyl, and T. Engman, "Measuring soil moisture with imaging radar," *IEEE TGRS*, vol. 33, pp. 915-926, 1995.
- [30] Z. Su, P. A. Troch, and F. P. De Troch, "Estimation of surface soil moisture by inversion of SAR data, surface scattering from random rough, bare soils, spatial and temporal soil moisture mapping from ERS-1/2, and JERS-1 SAR data and macroscale hydrologic modeling for regional climate models (RCM)," ESA, Noordwijk, The Netherlands, ESA Project A02-B106, 1997.
- [31] Q. Li and J. Shi, "A generalized power law spectrum and its implications to the backscattering of soil surfaces based on the integral equation model," *IEEE TGRS*, vol. 40, no. 2, pp. 270-280, Feb 2002.
- [32] N. F. Glenn and J. R. Carr, "Establishing a relationship between soil moisture and RADARSAT-1 SAR data obtained over the Great Basin Nevada, USA," *Can. J. Remote Sens.*, vol. 30, no. 2, pp. 176-181, 2004.
- [33] Y. Oh, K. Sarabandi, and F. T. Ulaby, "An empirical model and an inversion technique for radar scattering from bare soil surfaces," *IEEE TGRS*, vol. 30, no. 2, pp. 370-381, 1992.
- [34] Y. Zhang and S. Okamura, "New density-independent moisture measurements using microwave phase shifts at two frequencies," *IEEE TIM*, vol. 48, no. 12, pp. 1208-1211, 1999.
- [35] Z. Aly, F. J. Bonn, and R. Magagi, "Analysis of the backscattering coefficient of salt-affected soils using modeling and RADARSAT-1 SAR data," *IEEE TGRS*, vol. 45, pp. 332-341, 2007.
- [36] Z. Aly, F. Bonn, and R. Magagi, "Modelling the backscattering coefficient of salt-affected soils: applications to Wadi el Natrun bottom, Egypt," *EARSeL Proceedings 3*, pp. 372-381, 2004.
- [37] Y. Shao, Q. Hu, H. Guo, Y. Lu, Q. Dong, and C. Han, "Effect of dielectric properties of moist salinized soils on backscattering coefficients extracted from RADARSAT image," *IEEE TGRS*, vol. 41, pp. 1879-1888, 2003.
- [38] Z. M. Abdel-Razak, F. Bonn, L. P. Giugni, and A. Mahmood, "Potentiality of RADARSAT-1 images in the detection of salt affected soils in the arid zone: Wadi El-Natrun, Egypt," *Proceedings of IGARSS 2003*.
- [39] Y. Lasne, Ph. Paillou, Th. August-Bernex, G. Ruffié, and G. Grandjean, "A phase signature for detecting wet subsurface structures using polarimetric L-band SAR," *IEEE TGRS*, vol. 42, pp. 1683-1694, 2004.
- [40] A. K. Fung, Z. Li, K. S. Chen, "Backscattering from a randomly rough dielectric surface," *IEEE TGRS*, vol. 30, pp. 356-369, 1992.
- [41] C. Y. Hsieh, A. K. Fung, G. Nesti, A. J. Sieber, and P. Coppo, "A further study of the IEM surface scattering," *IEEE TGRS*, vol. 35, pp. 901-909, 1997.
- [42] T. D. Wu, and K. S. Chen, "A reappraisal of the validity of the IEM model for backscattering from rough surfaces," *IEEE TGRS*, vol. 42, pp. 743-753, 2004.
- [43] N. J. Tosca, S. M. McLennan, B. C. Clark, J. P. Grotzinger, J. A. Hurowitz, B. L. Jolliff, A. H. Knoll, C. Schröder, S. W. Squyres, "Geochemical modeling of evaporites on Mars: Insight from Meridiani Planum," Workshop LPS XXXVI, 2005.
- [44] W. C. Feldman, T. H. Prettyman, S. Maurice, J. J. Plaut, and D. L. Bish, "Global distribution of near surface hydrogen on Mars," *J. Geophys. Res.*, vol. 109, pp. 1-13, 2004.
- [45] I. G. Mitrofanov, M. L. Litvak, A. S. Kozyref, A. B. Sanin, V. Tretyakov, and W. V. Boynton, "Vertical distribution of shallow water in Mars subsurface from HEND/Odyssey data," *Microsymposium 38*, MS069, 2003.
- [46] D. T. Möhlmann, "Water in the upper Martian surface at mid- and low-latitude: presence, state, and consequences," *Icarus*, vol. 168, pp. 318-323, 2004.
- [47] C. B. Hunt, and D. R. Mabey, "General geology of Death Valley, California - Stratigraphy and structure, Death Valley, California: stratigraphy and structural geology, both of the surficial deposits and bedrock," U. S. Geological Survey Prof. Paper 494-A, Washington D. C., 162 p., 1966.
- [48] J. R. Knott, A. M. Sarna-Wojcicki, M. N. Machette, and R. E. Klinger, "Upper Neogene stratigraphy and tectonics of Death Valley - a review," *Earth Science Review*, vol. 73, pp. 245-270, 2005.
- [49] M. B. Miller, and T. L. Pavlis, "The Black Mountains turtlebacks: Rosetta stones of Death Valley tectonics," *Earth Science Reviews*, vol. 73, pp. 115-138, 2005.
- [50] M. B. Miller, "Geological landscapes of Death Valley region," *Earth Science Reviews*, vol. 73, pp. 17-30, 2005.
- [51] J. K. Crowley, and S. J. Hook, "Mapping playa evaporite minerals and associated sediments in Death Valley, California, with multispectral thermal infrared images," *JGR*, vol. 101, pp. 643-660, 1996.
- [52] C. B. Hunt, T. W. Robinson, W. A. Bowles, and A. L. Washburn, "General geology of Death Valley, California - Hydrologic basin, Death Valley, California: a description of the hydrology, geochemistry, and patterned ground of the saltpan," U. S. Geological Survey Prof. Paper 494-B, Washington D. C., 138 p., 1966.
- [53] M. A. Kohler, T. J. Nordenson, and D. R. Baker, "Evaporation maps for the United States," U. S. Weather Bureau Tech. Paper 37, 13 p., 1959.
- [54] M. A. Kohler, T. J. Nordenson, and W. E. Fox, "Evaporation from pans and lakes," U. S. Weather Bureau Research Paper 38, 21 p., 1955.
- [55] J. M. Rouchy, and M. M. Blanc-Valleron, *Les Evaporites*, Vuibert, 208p, 2006, in french.
- [56] E. Bouynet, *Ph.D. Thesis*, University of Bordeaux 1, 132p, 1996, in french.
- [57] T. P. Marsland and S. Evans, "Dielectric measurement with an open-ended coaxial probe," *Proceedings IEEE*, 134, 341-349, 1987.
- [58] G. B. Gadja and S. S. Stuchly, "An equivalent circuit of an open-ended coaxial line," *IEEE Trans. Instrumentation and Measur.*, IM32(4), pp. 506-508, 1983.
- [59] J. L. Miane and M. Ech-Chaoui, "," *Revue des Composites et des Matériaux Avancés*, vol. 2, pp. 115, 1992, in french.
- [60] M. A. Stuchly, S. S. Stuchly, M. M. Brady, and G. B. Gadja, "Equivalent circuit of an open-ended coaxial line in a lossy dielectric," *IEEE Trans. Instr. Meas.*, vol. 31, pp. 116-119, 1982.
- [61] J. P. Pérez, R. Carles, and R. Fleckinger, *Electromagnétisme*, Masson, 776p, 1997, in french.
- [62] J. J. van Zyl, and Y. Kim, "A quantitative comparison of soil moisture inversion algorithm," *Proceedings of IGARSS'01*, vol. 1, pp. 37-39, 2001.
- [63] E. Ceraldi, G. Franceschetti, A. Iodice, and D. Riccio, "Estimating the soil dielectric constant via scattering measurements along the specular direction," *IEEE TGRS*, vol. 43, pp. 295-305, 2005.
- [64] Y. Lasne, Ph. Paillou, G. Ruffié, and M. Crapeau, "Effect of multiple scattering on the phase signature of wet subsurface structures: Applications to polarimetric L- and C-band SAR," *IEEE TGRS*, vol. 43, pp. 1716-1726, 2005.
- [65] K. S. Chen, T. D. Wu, M. K. Tsay, and A. K. Fung, "A note on the multiple scattering in an IEM model," *IEEE TGRS*, vol. 38, pp. 249-256, 2000.



Yannick Lasne received the Astrophysics, Planetology and Space Techniques D.E.A. degree, and the Ph.D. degree in planetary geology and radar remote sensing from the University Paul Sabatier, Toulouse, France, in 2002 and 2005 respectively.

His scientific research interests concern remote sensing of arid regions, and the electromagnetic characterization of geological materials for soil moisture detection and cartography of the paleohydrology with applications to Mars exploration. His recent activities relates to the geological processes of evaporitic environments for soil moisture detection and mapping, as related to the dielectric properties of saline deposits.



Philippe Paillou received the Engineer Diploma from the Ecole Nationale Supérieure de Physique de Strasbourg, Strasbourg, France, in 1989, and the Ph.D. degree in image processing from the Université Louis Pasteur de Strasbourg, Strasbourg, France, in 1992.

Since September 2004, he has been a Professor at the University of Bordeaux, Bordeaux, France, and has been a Researcher at the Observatoire Aquitain des Sciences de l'Univers (OASU), Bordeaux, since 1998.

His research activities concern application of SAR to relief reconstruction, surface roughness measurement, and subsurface imaging. He is a Principal Investigator for several national and international projects related to radar remote sensing.



Anthony Freeman (M'83, SM '94, F '00) received the B.Sc. (Hons.) degree in mathematics in 1979 and the Ph. D. degree in astrophysics in 1982, both from the University of Manchester Institute of Science and Technology, Manchester, England.

Dr. Freeman is currently the Earth Science Research and Advanced Concepts Program Manager at the Jet Propulsion Laboratory (JPL). JPL has a broad portfolio of Earth Science missions as well as planetary science missions and this office is responsible for all of JPL's future work in this area. Prior to this position, he was section manager of the Mission and Systems Architecture Section at JPL, responsible for all advanced mission studies at JPL and prior to that instrument manager for the LightSAR Radar Program at JPL. His research interests include correction of Faraday rotation, modeling of polarimetric radar scattering signatures, and the design of P-Band spaceborne SARs.

He has been awarded the NASA Exceptional Service Medal for calibration of SIR-C mission data, numerous NASA new technology awards, and holds two patents.



Tom Farr received Bachelor's and Master's degrees from Caltech, and a PhD from the University of Washington, all in Geology. After a short time as an engineering geologist, he joined the Radar Sciences Group at the Jet Propulsion Lab, where he has been since 1975. At JPL, he helped develop the first geologic applications of imaging radar using aircraft, satellites, and the Space Shuttle. He has also been a science investigator on European and Japanese satellite programs and has assisted in the interpretation of radar images from Venus and recently from Saturn's moon Titan. His scientific research includes the use of remote sensing and digital topographic data for study of desert landscapes on Earth and Mars and how they are formed and modified by climate and tectonic or volcanic activity.



Kyle C. McDonald (S'89-M'91-SM'98) received the B.S. degree in electrical engineering (cooperative plan with highest honors) from the Georgia Institute of Technology, Atlanta, in 1983, the M.S. degree in numerical science from Johns Hopkins University, Baltimore, MD, in 1985, and the M.S. and Ph.D. degrees in electrical engineering from the University of Michigan, Ann Arbor, in 1986 and 1991, respectively.

He has been a Research Scientist in the Water and Carbon Cycles Group, Earth Science Division, Jet Propulsion Laboratory, California Institute of Technology, Pasadena, since July 2001. He specializes in electromagnetic scattering and propagation, with emphasis on microwave remote sensing of terrestrial ecosystems.

He has been a Principal and Co-Investigator on numerous National Aeronautics and Space Administration (NASA) Earth Science investigations. He is a member of the NASA's North American Carbon Program science team, the National Science Foundation's Pan-Arctic Community-Wide Hydrological Analysis and Monitoring Program Science Steering Committee, and the Advanced Land Observation Satellite Phased Array L-band Synthetic Aperture Radar Kyoto and Carbon Initiative science panel. He has been a member of the NASA Boreal Ecosystem-Atmosphere Study (BOREAS) and BOREAS Follow on science teams, the NASA Scatterometer/Asian Dust and Ocean Ecosystem instrument team, the NASA Ocean Vector Winds Science Team, and the NASA Cold Land Processes Steering Committee.

His research interests have primarily involved the application of microwave remote sensing techniques for monitoring seasonal dynamics in boreal ecosystems, as related to ecological and hydrological processes and the global carbon and water cycles. His recent activities have included development of radar instrumentation for measuring sea ice thickness from airborne platforms.



Gilles Ruffié received the Ph.D. degree in Electronics mention Microwaves, in 1987.

Since 1995, he has been with the IMS-MCM laboratory as instrumentation manager at the University of Bordeaux 1, France.

His research activities concern the electromagnetic characterization of materials.



Bruce Chapman received the A.B. in both physics and astronomy from the University of California, Berkeley, in 1981, and the Ph.D. from the Earth, Atmospheric, and Planetary Sciences Department, Massachusetts Institute of Technology, Cambridge, in 1986.

He has been with the Jet Propulsion Laboratory (JPL), Pasadena, CA, since 1986. He is currently a Principal Investigator in the Global RainForest Mapping Project (GRFM), sponsored by the National Space Development Agency of Japan NASDA, a Co-Investigator and Task Manager for the JERS-1 Amazon Multimission Mapping Study (JAMMS), a Co-Investigator and Task Manager for the Tropical Rain Forest Information Center [a prototype Earth Science Information Partnership (ESIP)], and a member of the Alaska SAR Facility User Working Group (ASFUWG). He spent two years working on the polarimetric SAR signal processor for the Airborne Synthetic Aperture Radar (AIRSAR) Group. He is the developer of the NASA/JPL imaging radar home page, including the SIR-C, LightSAR, and GRFM web sites. He was a member of the calibration team responsible for the polarimetric calibration of SIR-C data and has received three NASA group achievement awards.